

TATi-Thermodynamic Analytics ToolIt: TensorFlow-based software for posterior sampling in machine learning applications

Frederik Heber, Zofia Trstanova, Benedict Leimkuhler

August 30, 2022

Abstract

We describe a TensorFlow-based library for posterior sampling and exploration in machine learning applications. TATi, the Thermodynamic Analytics ToolIt, implements algorithms for 2nd order (underdamped) Langevin dynamics and Hamiltonian Monte Carlo (HMC). It also allows for rapid prototyping of new sampling methods in pure *Python* and supports an ensemble framework for generating multiple trajectories in parallel, a capability that is demonstrated by the implementation of a recently proposed ensemble preconditioning sampling procedure [56].

In addition to explaining the architecture of the Thermodynamic Analytics ToolIt and its connections with the *TensorFlow* framework, this article contains preliminary numerical experiments to explore the efficiency of posterior sampling strategies in ML applications, in comparison to standard training strategies. We provide a glimpse of the potential of the new toolkit by studying (and visualizing) the loss landscape of a neural network applied to the MNIST hand-written digits data set.

1 Introduction

The fundamental role of neural networks (NNs) is readily apparent from their widespread use in machine learning in applications such as natural language processing [72], social network analysis [26], medical diagnosis [6, 35], vision systems [66], and robotic path planning [44]. The greatest success of these models lies in their flexibility, their ability to represent complex, nonlinear relationships in high-dimensional data sets, and the availability of frameworks that allow NNs to be implemented on rapidly evolving GPU platforms [40, 29]. The industrial appetite for deep learning has led to very rapid expansion of the subject in recent years, although, as pointed out by Dunson [19], at times the mathematical and theoretical understanding of these methods has been swept aside in the rush to advance the methodology.

The potential impact on society of machine learning algorithms demands that their exposition and use be subject to the highest standards of clarity, ease of interpretation, and uncertainty quantification. Typical NN training seeks to optimize the parameters of the network (biases and weights) under the constraint that the training data set is well approximated [28, 23]. In the Bayesian setting, the parameters of a neural network are defined by the observations, but only in the probabilistic sense, thus specific parameter values are only realized as modes or means of the associated distribution, which can require substantial computation. Bayesian approaches based on exploration of the posterior probability distribution have been discussed throughout the development of neural networks [54, 59, 31, 2], and underpin much of the work in this field, but they are less commonly implemented in practice for “big data” applications due to legitimate concerns about efficiency [71]. While the idea of sampling (or partially sampling) the posterior of large scale neural networks is not new, improvements in computers continually render this goal more plausible. For a recent discussion, see the PhD thesis of Yarin Gal [22], which again champions the use of a (Bayesian) statistical framework, mentioning among other aims the prospect for meaningful uncertainty quantification in deep neural networks. The primary goal of the Thermodynamic Analytics ToolIt (TATi) is to facilitate the sampling of the posterior parameter distribution of automated machine learning systems with a balance of ease of use and computational efficiency, by leveraging highly optimised computational procedures within *TensorFlow*.

The now-standard framework for Bayesian parameterization relies on Markov Chain Monte Carlo methods, but these can be difficult to scale to large system system. In the context of deep learning, we use the term *large* to refer both to large data set size (which translates into expensive likelihood computations) and to large numbers of parameters (usually the consequence of adopting a *deep learning*

paradigm). We base our software on discretized stochastic differential equations which offer a reliable and accurate means of computing Markov Chain Monte Carlo (MCMC) sampling paths while providing rigorous results with statistical error bounds [49].

As an indication of the possible scope for practical posterior sampling in large scale machine learning, we note that Markov Chain Monte Carlo methods like those implemented in TATi have been successfully deployed in the more mature setting of very large scale molecular simulations in computational sciences for applications in physics, chemistry, material science and biology, with variables numbering in the millions or even billions [39, 74, 36]. The goal in molecular dynamics is similarly the sampling of a target probability distribution, although the distribution typically arises from semi-empirical modelling of interactions among atoms of the substances of interest. The scientific communities in molecular sciences are developing highly efficient “enhanced sampling” procedures to tackle the computational difficulties of large scale sampling (see the surveys [21, 3] for some examples of the wide variety of methods being used in biomolecular applications). In analogy with molecular dynamics, the focus on posterior sampling makes possible the elucidation of reduced descriptions of neural networks through concepts such as free energy calculation [50] and transition path sampling [5]. Although we reserve detailed study of these ideas for future work, the fundamental tool in their construction and practical implementation is the ability to compute sample sequences efficiently and reliably using MCMC paths, such as produced by the TATi library. Further potential benefits of the posterior sampling approach lie in the fact that it offers a means of high-dimensional uncertainty quantification through standard statistical methodology [68, 22].

The emphasis in TATi is on methods that derive from a discretization of underdamped Langevin dynamics. This is a framework that incorporates auxiliary momentum variables. Such schemes have excellent properties in terms of accuracy of statistical averages and convergence rates [49, 50]. A variety of other schemes which are also based on second order dynamics could eventually be implemented in TATi without significant difficulty [10, 62, 67, 55]. In fact, one of the purposes of TATi is to provide a relatively simple mechanism for the implementation and evaluation of sampling strategies of statistical physics in machine learning applications. While *TensorFlow*’s graph programming structure is well explained and motivated by its developers and provides efficient execution on GPUs, it is not straightforward for numerical analysts, statisticians and statistical physicists to modify in order to test their methods. As we explain in Section 3 of this article, TATi uses a simplified interface structure that allows algorithms to be coded directly in pure *Python* and then linked to *TensorFlow* for efficient calculation of gradients for arbitrary *TensorFlow* models. As a consequence, building and testing a new sampling scheme in TATi requires little knowledge of the underpinnings of *TensorFlow*. Within TATi we provide detailed user’s guide and programmer’s manual to further improve uptake.

Another goal we have had in mind with TATi is to improve the understanding of the loss landscape (given by the log of the posterior density) so as to better understand its structure vis a vis the performance of parameterization algorithms. The loss is not convex in general [43, sect. 4], and its corrugated (“metastable”) structure has been compared to models of spin-glasses [12]: there is a band of minima close to the global minimum as lower bound and whose multitude diminishes exponentially for larger loss values. The availability of an efficient sampling scheme gives a means of better understanding the loss landscape and its relation to the network (and properties of the data set). We illustrate some of the potential for such studies in Section 5 of this article, where we examine the loss landscape of an MNIST classification problem.

TensorFlow recently¹ has added a `probability` module that among other things extends it by an MCMC framework. While this MCMC framework is very powerful for general purpose sampling, it is rather aimed at sampling tasks for which the exact gradient can be easily computed. Even though it can be used to sample the log posterior of neural networks in principle, it does not provide anything like TATi’s simple interface and contains only a small subset of TATi’s sampling schemes. Although it features both a Hamiltonian Monte Carlo (HMC) and an Stochastic Gradient Langevin Dynamics (SGLD) sampler, these are implemented using different paradigms, one based on the MCMC framework while the other derives from *TensorFlow*’s `Optimizer` class. As mentioned in Secs. 3 and 4, the implementations introduce certain constraints on dataset access. Finally we highlight the need for a framework that can be extended using Python implementation of enhanced sampling algorithms readily accessible in the statistics and physics communities, in comparison with the less familiar *TensorFlow* alternatives.

TATi has the potential for broad impact in several research areas related to NN construction. In particular, the ability to sample the posterior distribution efficiently will we anticipate help to address challenges such as: the relationship between network architecture and parameterization efficiency (see

¹released April 2018

Safran and Shamir [65], Livni et al. [53], Haeffele and Vidal [27], Soltanolkotabi et al. [69]), the visualization of the loss manifold and the parameterization process (see Draxler et al. [17], Im et al. [34], Li et al. [52], Goodfellow et al. [23]), and the assessment of the generalization capability of networks (see Dinh et al. [16], Hochreiter and Schmidhuber [32], Kawaguchi et al. [37], Hoffer et al. [33]).

Finally, we note that the statistical perspective underpins many optimization schemes in current use in machine learning, such as the Stochastic Gradient Descent (SGD) method. The stochasticity enters into this method through the subsampling of the dataset at every iteration of the optimization algorithm, due to so-called ‘minibatching’. Several stochastic optimisation methods have been proposed aiming at improving the computational efficiency or reducing generalisation error, e.g., RMSprop [30], AdaGrad [18], Adam [38], entropy-SGD [9]. Stochastic gradient Langevin dynamics (SGLD) [71], similarly, can be given a statistical (sampling) interpretation. Indeed, when its stepsize is held fixed and under simplifying assumptions on the character of the gradient noise, it can be viewed as a first-order discretization of overdamped Langevin dynamics. We discuss SGD and SGLD in Sec 2, in order to motivate the sampling framework.

The remainder of this paper is structured as follows: Section 2 provides an introduction to MCMC, Langevin dynamics schemes and the concepts from numerical error analysis that underpin TATi. We also briefly outline there the Ensemble Quasi-Newton method of [56]. In Section 3 we discuss the TATi toolkit architecture and each of its component parts. We then benchmark TATi’s performance in some test cases in Section 4. Finally, we elaborate on how TATi can be used to handle moderate-dimensional sampling on the MNIST dataset in Section 5. Large scale experiments with state-of-the-art applications are the subject of current research of the authors and will be reported elsewhere.

2 Markov Chain Monte Carlo methods and stochastic differential equations

In this section, we provide a brief introduction to the MCMC methods used for sampling high dimensional distributions, particular the stochastic. These methods include schemes based on discretization of stochastic differential equations, especially Langevin dynamics. We discuss in some detail the construction of numerical schemes in order to control the finite time stepsize bias. Moreover, we describe an HMC algorithm as implemented in TATi and an ensemble quasi-Newton method that adaptively rescales the dynamics to enhance sampling of poorly conditioned target posteriors.

We assume that we are given a dataset $\mathcal{D} = (\mathcal{X}, \mathcal{Y}) = \{(x_i, y_i)\}_{i=1}^M$ comprising inputs and outputs of an unknown functional relationship. We also assume we are given a neural network defined by a vector of parameters $\theta \in \Omega \subset \mathbb{R}^N$ which acts on an input $x \in \mathcal{X}$ to produce output $f(x, \theta)$. The goal of training the network is then typically formulated as solving an optimization problem over the parameters given the dataset:

$$\min_{\theta \in \mathbb{R}^N} L(\theta, \mathcal{D}), \quad (1)$$

where the function $L(\theta, \mathcal{D})$ is the total loss function associated to the dataset \mathcal{D} , defined by

$$L(\theta, \mathcal{D}) = \sum_{(x,y) \in \mathcal{D}} l(f(x, \theta), y) = \sum_{i=1}^M l(f(x_i, \theta), y_i). \quad (2)$$

The loss function $l(\hat{y}, y)$ depends on the metric choice, for example the squared error, logarithmic loss, cross entropy loss, etc [64]. The total loss is in general not a convex function even though l may be convex. This gives rise to many local minima in the loss manifold $L(\theta, \mathcal{D})$, see [12].

The parametrization procedure is based on optimization algorithms, which generate a sequence of parameter vectors $\theta_0, \theta_1, \dots, \theta_k, \dots$, converging to a (local) minimizer of (1) as $k \rightarrow \infty$. The basic optimization algorithm is the Gradient Descent (GD), which uses the negative gradient to update the parameter values, i.e.,

$$\theta_{k+1} = \theta_k - \varepsilon \nabla L(\theta_k), \quad (3)$$

where ε is the stepsize (or learning rate), which is either constant or may be varied during the computation. GD converges for a convex function and for a smooth non-convex total loss function it converges to the nearest local minimum [60].

Gradient calculations are the primary computational burden when training neural networks, i.e., the computational cost of a gradient can be taken as a reasonable measure of computational work. As the total loss L implicitly depends on the whole dataset, one natural idea that reduces the computational

cost is to exploit the redundancy in the dataset by estimating the gradient of the average loss from a subset of the data, that is, to replace the gradient in each parameterization step by the approximation

$$\nabla \tilde{L}(\theta) \approx \frac{M}{m} \sum_{i \in S_k} \nabla l(f(x_i, \theta), y_i).$$

Where S_k represents a randomized data subset (re-randomized throughout the training process) of dimension m , this method, which has many variants, is referred to as SGD.

We are interested in the Bayesian inference formulation, where θ is the parameter vector and we wish to sample from the posterior distribution $\pi(\theta | \mathcal{D})$ of the parameters given a dataset of size $M > 0$,

$$\pi(\theta | \mathcal{D}) \propto \pi_0(\theta) \prod_{i=1}^M \pi((x_i, y_i) | \theta),$$

with prior probability density $\pi_0(\theta)$, and likelihood $\pi((x, y) | \theta)$.

Stochastic Gradient Langevin Dynamics (SGLD) [71] generates a step based on a subset of the data and injects additional noise. The SGLD parameter update is using a sequence of stepsizes $\{\varepsilon_n\}$ and reads

$$\theta_{k+1} = \theta_k - \varepsilon_k \nabla \tilde{L}(\theta_k) + \sqrt{2\beta^{-1}\varepsilon_k} G_k, \quad (4)$$

with

$$\nabla \tilde{L}(\theta) = -\beta^{-1} \nabla \log(\pi_0(\theta)) - \beta^{-1} \frac{M}{m} \prod_{i \in S_k} \nabla \log(\pi((x_i, y_i) | \theta))$$

where $\beta > 0$ is a constant (in physics, it would be associated with reciprocal temperature) and again S_k is a random subset of indices $1, \dots, M$ of size m . The original algorithm uses a diminishing stepsize sequence, however, [70] showed that fixing the stepsize has the same efficiency, up to a constant.

Under the assumption that the gradient noise is uncorrelated and identically distributed from step to step, it is easy to demonstrate that SGLD with fixed stepsize is an Euler-Maruyama (first order) discretization of overdamped Langevin dynamics [71]:

$$d\theta = -\nabla \tilde{L}(\theta) dt + \sqrt{2\beta^{-1}} dW_t. \quad (5)$$

This creates a natural starting point for our approach: we simply change the perspective to focus on the sampling of the posterior distribution, rather than the identification of its mode.

In case a full gradient is used, dynamics (5) preserves the Boltzmann distribution with measure proportional to an exponential function of the negative loss:

$$\pi(d\theta) \propto e^{-\beta L(\theta)} d\theta. \quad (6)$$

Given a generic process providing samples θ_k asymptotically distributed with respect to a defined target measure π , it is possible to use sampling paths to estimate integrals with respect to π . Define the finite time average of a C^∞ function φ by

$$\hat{\varphi}(K) := \frac{1}{K+1} \sum_{k=0}^K \varphi(\theta_k).$$

For an ergodic process, we have

$$\lim_{K \rightarrow \infty} \hat{\varphi}(K) = \int_{\Omega} \varphi(\theta) \pi(d\theta). \quad (7)$$

The convergence rate of the limit above is given by the Central Limit Theorem (CLT). Given a generic process generating samples θ_k from a target distribution with density π , the variance of an observable φ behaves, asymptotically for large K , as

$$\text{var } \hat{\varphi}(K) \sim \tau_\varphi \text{var } \varphi / K$$

where τ_φ is the *integrated autocorrelation time* (Integrated Autocorrelation Time (IAT)) see [25, sect. 3]. τ_φ can be viewed as a measure of the redundancy of the sampled values or the number of steps until the sampled values of φ decorrelate, thus $\tau_\varphi = 1$ is optimal, i. e., immediately stepping from one independent state to the next. The IAT τ_φ can also be calculated as

$$\tau_\varphi = 1 + 2 \sum_1^\infty \frac{C_\varphi(k)}{C_\varphi(0)} \quad \text{with} \quad C_\varphi(k) = \text{cov}[\varphi(\theta_k), \varphi(X_0)], \quad (8)$$

where the covariance is averaged over the initial condition.

In practice, in some of the schemes implemented in TATi, the process of discretization of the SDE introduces asymptotic bias, which is controlled by the stepsize, however it is nonetheless possible and useful to compute the IAT in such a case to describe the convergence to the asymptotically perturbed equilibrium distribution.

Langevin Dynamics. Sampling from (6) is one of the main challenges of computational statistical physics. There are three popular alternative approaches to sample from (6): discretization of continuous stochastic differential equations (SDEs), Metropolis-Hastings based algorithms and deterministic dynamics, as well as combinations among the three groups. TATi implements methods of each type.

Langevin dynamics is an extended version of (5):

$$\begin{cases} d\theta_t = M^{-1}p_t dt, \\ dp_t = -\nabla L(\theta_t) dt - \gamma M^{-1}p_t dt + \sigma dW_t, \end{cases} \quad (9)$$

where p is the momentum variable and $\gamma > 0$ is the friction. The fluctuation-dissipation relation $\sigma^2 = \frac{2\gamma}{\beta}$ ensures that the extended (canonical) distribution with density

$$\pi_{\text{ext}} \propto \exp[-\beta (p^T M^{-1}p/2)] \pi(\theta)$$

is preserved; the target distribution is recovered by marginalization. Whereas the momentum is a physical variable in statistical mechanics, it is introduced as an artificial auxiliary variable in the machine learning application. M in (9) is a positive definite mass matrix, which can in many cases be taken to the identity matrix.

The discretization of stochastic dynamics introduces bias in the invariant distribution (see below, for discussion). Although the bias can be removed through the incorporation of a Metropolis-Hastings (MH) step, such methods do not always scale well with the dimension [4, 63]; and the MH test is often neglected in practice. For example the “unadjusted Langevin algorithm” of [20] tolerates the presence of small stepsize-dependent bias, in order to obtain faster convergence (reduced asymptotic variance or lower integrated autocorrelation time for observables of interest) and better overall efficiency.

In TATi, we emphasize Langevin dynamics discretizations but TATi includes a Hamiltonian Monte Carlo method (see below) which we briefly test in this article; the Metropolis scheme implemented in TATi’s HMC could be adapted to other, more general proposal distributions.

Systematic design of schemes. The mathematical foundation for the construction of discretization schemes for (9) by splitting of the generator of the dynamics is now well understood [49]. Although different choices can be made, the usual starting point is an additive decomposition of the generator of dynamics (9) into three operators $\mathcal{L} = A + B + O$, where

$$A := M^{-1}p \cdot \nabla_{\theta}, \quad B := -\nabla L(\theta) \cdot \nabla_p, \quad O := -\gamma M^{-1}p \cdot \nabla_p + \sigma \Delta_p, \quad (10)$$

The main idea is that each of these sub-dynamics can be resolved exactly in the weak (distributional) sense. Note that the (“O” step) dynamics

$$dp_t = -\gamma M^{-1}p_t dt + \sigma dW_t, \quad (11)$$

has an analytical solution

$$p_t = \alpha_t p_0 + \sigma \int_0^t \alpha_{t-s} dW_s, \quad \alpha_t := e^{-\gamma M^{-1}t}. \quad (12)$$

A Lie-Trotter splitting of the elementary evolution generated by A, B , and O provides six possible first-order splitting schemes of the general form

$$P_{\varepsilon}^{Z,Y,X} = e^{\varepsilon Z} e^{\varepsilon Y} e^{\varepsilon X},$$

with all possible permutations (Z, Y, X) of (A, B, O) , and second-order splitting schemes are then obtained by a Strang splitting of the elementary evolutions generated by A, B , and O .

Using the notation for the three operators of the sub-dynamics (10), we define the following updates which will be combined in the full scheme for the discretization of the Langevin dynamics with stepsize ε :

$$\begin{aligned} A_{\varepsilon} &: \theta \rightarrow \theta + \varepsilon p, \\ B_{\varepsilon} &: p \rightarrow p - \varepsilon \nabla L(\theta), \\ O_{\varepsilon} &: p \rightarrow ap + \sqrt{\beta^{-1}(1-a^2)}R, \end{aligned} \quad (13)$$

with $a = e^{-\gamma\varepsilon}$ and $R \sim \mathcal{N}(0, 1)$. A numerical methods is easily specified by a string such as ‘ABO’. This is an instance of the Geometric Langevin Algorithm [8]. We also consider symmetric compositions of several basic steps. The ‘BAOAB’ scheme is in this notation $B_{\varepsilon/2}A_{\varepsilon/2}O_{\varepsilon}A_{\varepsilon/2}B_{\varepsilon/2}$. This method can be written out in detail as a step from (θ_k, p_k) to (θ_{k+1}, p_{k+1}) as follows:

$$\begin{aligned} p_{k+1/2} &= p_k - \frac{\varepsilon}{2} \nabla L(\theta_k), \\ \theta_{k+1/2} &= \theta_k + \frac{\varepsilon}{2} M^{-1} p_{k+1/2}, \\ p_{k+1} &= \alpha p_{k+1/2} + \sqrt{\beta^{-1}(1 - \alpha^2)} R_{k+1/2}, \\ \theta_{k+1} &= \theta_{k+1/2} + \frac{\varepsilon}{2} M^{-1} p_{k+1}, \\ p_{k+1} &= p_{k+1/2} - \frac{\varepsilon}{2} \nabla L(\theta_{k+1}). \end{aligned}$$

Given the sequence of samples (θ_k, p_k) determined using such a method, we can approximate expected values of a C^∞ function of θ and p using the standard estimator based on trajectory averages

$$\widehat{\varphi}_K = \frac{1}{K+1} \sum_{k=0}^K \varphi(\theta_k, p_k). \quad (14)$$

It can be shown in certain cases that these discrete averages converge to an ensemble average,

$$\lim_{K \rightarrow \infty} \widehat{\varphi}_K = \int_{\Omega} \varphi(\theta, p) d\pi_\varepsilon(\theta, p) = \mathbb{E}_{\pi_\varepsilon}(\varphi),$$

where π_ε represents the stationary density of the (biased) discrete process. Under specific assumptions on the splitting scheme [49], an expansion may be made in the time stepsize of the invariant measure of the splitting scheme which guarantees that the error in an ergodic approximation of an observable average is bounded relative to ε^q , where q depends on the detailed structure of the numerical method. Thus

$$\mathbb{E}_{\pi_\varepsilon}(\varphi) = \mathbb{E}_{\pi_{\text{ext}}}(\varphi) + O(\varepsilon^q).$$

Schemes such as ‘ABO’ can be shown to be first order ($q = 1$), whereas BAOAB and ABOBA are second order. Delicate cancellations imply that BAOAB can exhibit an unexpected fourth order of accuracy in the ‘high friction’ limit ($\gamma \rightarrow \infty$) when the target is sampling of configurational (θ -dependent) quantities. The latter method also has remarkable features with respect configurational averages in harmonic systems and near-harmonic systems, see [47], Chapter 7, for more details.

All explicit Langevin integrators are subject to stability restrictions which require that the product of stepsize and the frequency of the fastest oscillatory mode is bounded.

Hybrid Monte Carlo Hybrid Monte-Carlo, also called Hamiltonian Monte Carlo, is a MCMC method based on the Metropolis-Hastings algorithm that allows one to sample directly from the target distribution π . Starting from an initial position (θ, p) , the momenta are re-sampled from $\mathcal{N}(0, M\beta^{-1})$ and a proposal $(\tilde{\theta}, \tilde{p})$ is obtained by evaluating K_{HMC} times the Verlet method, i.e., $B_{\varepsilon/2}A_{\varepsilon}B_{\varepsilon/2}$. The proposal is then accepted with a probability given by the Metropolis ratio:

$$\min\left(1, e^{-\beta(H(\tilde{\theta}, \tilde{p}) - H(\theta, p))}\right), \quad (15)$$

where the energy H is given by $H(\theta, p) = L(\theta, \mathcal{D}) + \frac{1}{2}p^T M^{-1}p$. In case the proposal is rejected, the state is reset to the starting point (θ, p) . The number of steps K_{HMC} is often randomized. The parameterization of this method depends on the trade-off between the larger time stepsizes ε and the number of steps K_{HMC} , implying higher rejection rates for the proposals and smaller stepsizes leading to potentially slow exploration of the parameter space.

Multiple walkers: the ensemble quasi-Newton method TATi includes support for propagating multiple ‘walkers’ (i.e., replicas) in parallel. This allows the implementation of more exotic sampling schemes which can give higher sampling efficiency. One such scheme is the preconditioned method developed in [56] which we refer to as the ‘ensemble quasi-Newton’ (EQN) method. The idea of this scheme is easily motivated by reference to a simple harmonic model problem in two space dimensions in which the stiffness (or frequency of oscillation) is very high in one direction and not in the other. The

stepsize for stable simulation using a Langevin dynamics strategy will be determined by the high frequency term meaning that the exploration rate suffers in the slowest direction. Effectively the integrated autocorrelation time in the “slow” direction is large compared to the timestep of dynamics.

In the harmonic case it is easy to rescale the dynamical system in such a way that sampling proceeds rapidly. In the more complicated setting of nonlinear systems in multiple dimensions, the idea that a few directions may restrict the progress of the sampling still has merit, but we no longer have direct access to the underpinning frequencies. The idea is to determine this rescaling adaptively and dynamically during simulation. There are several ways to do this in practice (see [42] for an early related work on using Hessian information to speed up convergence of GD).

In the paper of [56] modified dynamics is based on construction of the covariance matrix of the walker collection. This matrix is computed during simulation to determine the appropriate dynamical rescaling. The implementation is somewhat involved, thus making it an excellent test for TATi’s versatility and robustness. For details of the EQN scheme, the reader is referred to [56] (and, in particular, the *Python* code referenced within it).

We next describe the differential equations of the EQN scheme. Suppose we have L walkers (replicas). Denote by θ_i the position vector of the i th walker and by p_i the corresponding momentum vector, each of which is a vector in \mathbb{R}^N , where N is the number of parameters of the network. We assume that the mass matrix of the underlying system is the identity matrix, for simplicity. The equations of motion for the i th walker then take the form

$$d\theta_i = B_i(\theta)p_i dt, \quad (16)$$

$$dp_i = -B_i(\theta)^T \nabla L(\theta_i) dt + \text{div}(B_i(\theta)^T) dt - \gamma p_i dt + \sqrt{2\beta^{-1}\gamma} dW_i. \quad (17)$$

Here dW_i has the previous interpretation of a Wiener increment and div is the tensor divergence. The matrix B_i estimates the matrix square root of the covariance matrix which depends on the locations of all the walkers.

Under discretization, we compute steps in configurations $\theta_{k,i}$ and momenta $p_{k,i} \in \mathbb{R}^N$ at iteration step k with walker index i . We use a variant of the BAOAB discretization applied to walker i :

$$p_{k+1/2,i} = p_{k,i} - \frac{\varepsilon}{2} B_{k,i} \nabla L(\theta_{k,i}), \quad (18a)$$

$$\theta_{k+1/2,i} = \theta_{k,i} + \frac{\varepsilon}{2} B_{k+1/2,i} p_{k+1/2,i}, \quad (18b)$$

$$\hat{p}_{k+1/2,i} = \alpha p_{k+1/2,i} + \frac{(\alpha+1)\varepsilon}{2} \text{div}(B_{k+1/2,i}^T) + \sqrt{\frac{1-\alpha^2}{\beta}} R_{k,i}, \quad (18c)$$

$$\theta_{k+1,i} = \theta_{k+1/2,i} + \frac{\varepsilon}{2} B_{k+1/2,i} \hat{p}_{k+1/2,i}, \quad (18d)$$

$$p_{k+1,i} = \hat{p}_{k+1/2,i} - \frac{\varepsilon}{2} \nabla L(\theta_{k+1,i}). \quad (18e)$$

As in the code of [56], we make the calculation in (18b) explicit by updating $B_{k,i}$ only infrequently, typically every 1,000 steps, and we define $B_{k,i}$ by

$$B_{k,i} = \sqrt{\mathbf{1} + \eta \text{cov}(\theta_{k,[i]}, \theta_{k,[i]})}, \quad (19)$$

In the above, the matrix square root is understood in the sense of a Cholesky factorization, $\eta \geq 0$ is a covariance blending constant, and $\theta_{k,[i]}$ is the set of all walker positions at timestep k , excluding those of walker i itself. Note that for moderate η the choice (19) is always positive definite even if $L < N$. However, with (19) the affine invariance property, an elegant feature of the original system, no longer strictly holds. Nonetheless, the simplified method has been shown to work very well in practice [56, sect. 4].

3 TATi architecture

TensorFlow is a potent machine learning framework² that comes with a very distinct programming paradigm, namely the flow of computations results from a computational graph: A graph consists of

²We have picked *TensorFlow* as it has become a mature framework, backed by a large community. It has an open-source license and therefore is easy to extend beyond its given API. This is especially so with the duck-typed *Python* programming language. Also, *TensorFlow* gives an API stability promise for this language. Finally, it scales up to very large machines with GPU-assisted hardware and allows to tackle very large networks and datasets.

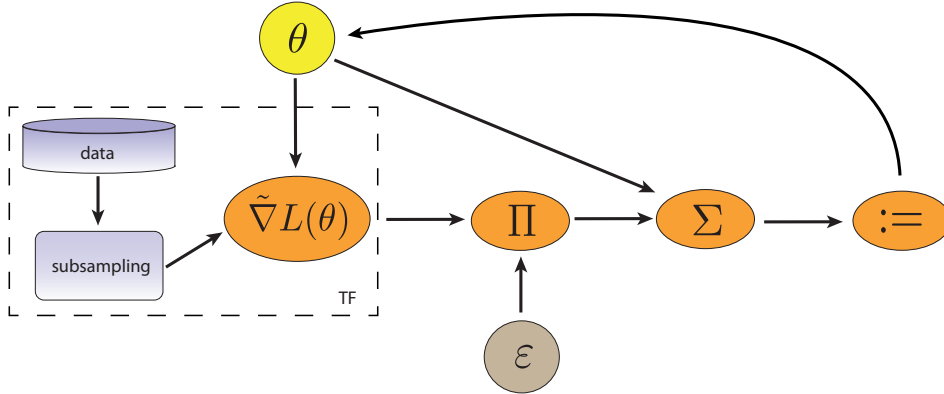


Figure 1: Visualization of the computation of a single step of a gradient descent algorithm $\theta := \theta + \varepsilon \nabla L(\theta)$. using the *TensorFlow* programming model: computation nodes (such as product operator Π and addition operator Σ) act on variables (e.g., the parameter vector θ) and coefficients such as the stepsize ε to produce a new parameter vector. Evaluating the assignment node at right triggers a single step. The approximate gradient computation is handled within TensorFlow’s autodifferentiation framework.

nodes and edges. Nodes symbolize operations such as summation, multiplication, assignment, picking a maximum components and many more, while edges represent the input/output flow in between these nodes. The flow itself consists of tensors of arbitrary modes of any of *Python*’s simple datatypes such as strings, floats, or integers. A *Python* program based on *TensorFlow* then contains instructions to set up this computational graph and to evaluate nodes in this graph.

In Figure 1 we illustrate the graph constructed for a GD update step. When the assignment node ($:=$) is triggered (e.g., by a `tensorflow.Session.run()` call), the graph is followed backwards until the only nodes encountered are placeholders (for user input), variables, or nodes whose (stateful) operation has been cached from a previous evaluation, i.e., tensors. Then, the tensors are transported forward, manipulated through the operation of each node, until the requested node, here the updated positions, can be evaluated. This is closely connected to Dynamic Programming, see for example the standard textbook by [14].

The encapsulation of operations in nodes and the dependency graph has the outstanding advantage that the parallelization of executions can be deduced directly from the graph structure.

TATi. There are two approaches to using Thermodynamic Analytics ToolIt (TATi), see Figure 2. On the one hand, it is a toolkit consisting of command-line programs such as TATiOptimizer, TATiSampler, TATiLossFunctionSampler, and TATiAnalyzer that, when fed a dataset and given the network specifics, is able to optimize and sample the network parameters and analyze the explored loss manifold. On the other hand, TATi can be readily used inside *Python* programs by using its modules: `simulation`, `model`, and `analysis`. The `simulation` module contains a very easy-to-use, high-level interface to neural network modelling, granting full access to the network’s parameters, its gradients, its loss and all other quantities of interest, see Listing 1 for an illustration. It is especially practical for rapid prototyping. The module `model` is its low-level counterpart and allows for implementations requiring more fine-grained control. Finally, `analysis` contains many classes to perform typical analysis tasks on sampled trajectories.

In light of the complexity of *TensorFlow*, we stress TATi’s ease-of-use feature. In the `simulation` module and the toolset all the intricacies of setting up neural network modelling are hidden away. The networks are simply specified by a set of options. Moreover, all that the user sees, especially when relying only on the `simulation` module of TATi, is a simple *Python* program in the familiar linear paradigm. The programmer instantiates a single class and calls upon its functions to request gradients, the current set of neural network parameters, to predict labels for a given set of features, and so on, again see Listing 1 for a lightweight example.

Listing 1: Example *Python* program using TATi’s `simulation` module: The `tati` interface instance `nn` contains the neural network and allows read&write access to its parameters as a single vector. Moreover, the current loss and the gradient with respect to the parameter set are requested.

```
import TATi.simulation as tati
import numpy as np
```

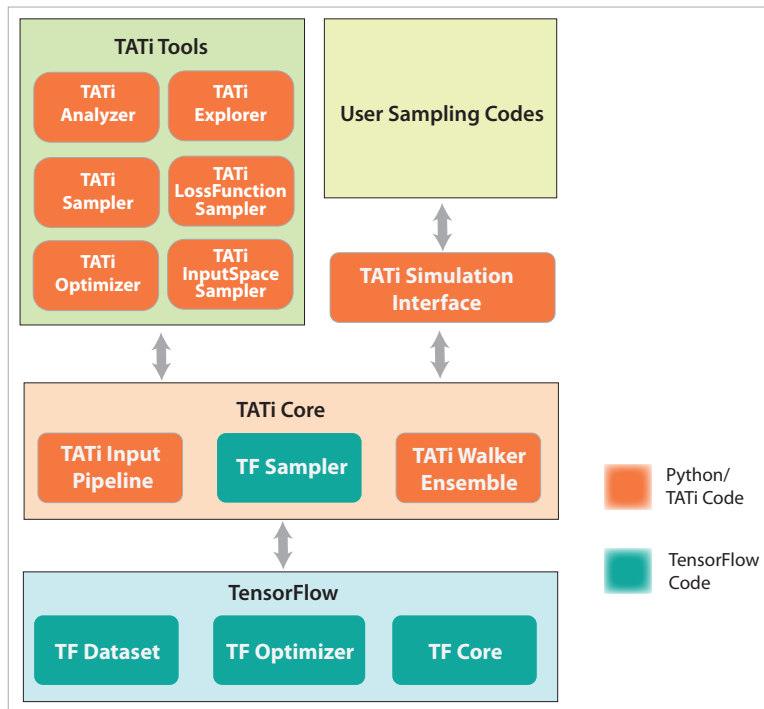


Figure 2: Architectural visualization of TATi’s modules and its toolset. The underlying functionality of *TensorFlow* is enhanced by TATi core components, supplying the user with a set of tools or modules to use in sampling. Each feature implemented in either *TensorFlow*’s computational graph paradigm or *Python*’s linear paradigm is highlighted in blue or orange, respectively.

```

# prepare parameters
nn = tati(
    batch_data_files=["dataset-twoclusters.csv"],
    batch_size=10,
    output_activation="linear"
)

# assign parameters of NN
nn.parameters = np.zeros((nn.num_parameters()))

# simply evaluate loss
nn.loss()

# also evaluate gradients (from same batch)
nn.gradients()

```

Finally, let us give a few examples to highlight our attention to detail when writing this toolkit:

TensorFlow recently also allows to add nodes dynamically to the graph (“eager execution”. In TATi we do not rely on this feature (promoted by *PyTorch* [61]), as it would prevent certain optimizations from being possible. Therefore, the graph is constructed a priori, then a `Session` object is instantiated that contains the temporary workspace for all graph nodes. Subsequently, this `Session` object is used to evaluate a given set of nodes in the graph that trigger the evaluation of others.

As a second example, we took extensive care to allow for reproducible runs by specifying a single random number generator seed. *TensorFlow* allows this on a local level and also on a global level but the latter only for static graphs. When any nodes are removed from or added to the computational graph, e.g., because of added functionality with a new version of TATi, all global random numbers change again. Moreover, during development of a program the graph may change frequently but the random number’s stability is crucial for testing purposes and reproducibility.

As we deemed reproducible runs essential also for scientific rigor, we could not rely on the well-known *Keras* interface to define the neural network topology as it offers no remedy to the reproducible random number issue. Instead we built a fully-connected multi-layer perceptron with dropouts from the bottom up by a set of parameters given by the user: The number of nodes per hidden layer, the activation function in the output and the hidden layers, the loss function, and so on. However, support for *Keras* is not excluded from future versions.

Table 1: Designation of the several samplers following the notation in Sec. 2. For the HMC, the MH evaluation is not shown, and l indicates that the number of leapfrog steps taken prior to accept/reject test.

Sampler	Dynamics	Designation
SGLD	Brownian	see (4)
GLA 1st order	Langevin	$B_\varepsilon A_\varepsilon O_\varepsilon$
GLA 2nd order	Langevin	$B_{\varepsilon/2} A_\varepsilon B_{\varepsilon/2} O_\varepsilon$
BAOAB	Langevin	$B_{\varepsilon/2} A_{\varepsilon/2} O_\varepsilon A_{\varepsilon/2} B_{\varepsilon/2}$
HMC	Hamiltonian	$(B_{\varepsilon/2} A_\varepsilon B_{\varepsilon/2})^l$

As a last example, the input pipeline is of especial importance in neural network computations as data needs to be channeled fast enough as input to the linear matrix operations of the network. Datasets may be too large for memory and need to be read from file in parts. Since *TensorFlow* version 1.4, there is a distinct `dataset` module to solve this efficiently. This module adds functions to add nodes to the computational graph that read the dataset from files and manipulate them to match the dimensionality and form required by the input layer and the output layer of the network. However, when developing code, smaller datasets typically suffice for testing. There, the module’s overhead may be wasteful. Therefore, we have added an extra "in-memory" input pipeline that uses `feed_dict` directly, see also section 4. The user can switch between the two by changing a single parameter. Note that the `dataset` module allows to replace an input layer of placeholders, used to feed the dataset’s features, with the node of an `iterator` supplying batches’ features of the dataset. However, this is both slower in our experiments (see also section 4.4) and it would have resulted in a loss of flexibility of the toolkit as the triggering of the next batch is now done automatically, namely exactly once per `tensorflow.Session.run()` call (as for all stateful operations).

Finally, we will briefly discuss in the following subsections three main highlights of TATi that we also mentioned in the beginning: new samplers, rapid prototyping, and ensemble methods.

3.1 Sampler

In TATi we aim for a balance between both performance and flexibility to accommodate any kind of sampling scheme. Moreover, we allow for sampling loss manifolds of very large networks and also very large datasets. Therefore, we have based all our samplers on the *TensorFlow*’s `Optimizer` class. An overview is given in table 1, see (4) for the SGLD method and (10) for details of the A,B,O operators mentioned here.

All of these sampling methods require a single force evaluation per time step. *TensorFlow*’s `Optimizer` class demands that it takes place at the beginning of each step. In order to match this requirement, the discrete time integration sequence associated to each sampler has been circularly permuted such that only a single force evaluation at the very beginning is required.

Let us illustrate this using the “BAOAB” method: In place of $B_{\varepsilon/2} A_{\varepsilon/2} O_\varepsilon A_{\varepsilon/2} B_{\varepsilon/2}$, the implementation in TATi computes $B_{\varepsilon/2} B_{\varepsilon/2} A_{\varepsilon/2} O_\varepsilon A_{\varepsilon/2}$ per sampling step with the force evaluation taking place the very beginning, before the first of the two “B” steps. In the unpermuted sequence the gradients would need to be recomputed before the last “B” step. In TATi this is delayed until the next sampling step where updated gradients are available.

The permuted algorithms behave identically to their unpermuted counterparts if started from an equilibrated position with zero gradients, which is the default case. Although the stability under iteration of the method is independent of permutation, it is important that properties, such as the kinetic energy, are evaluated at the appropriate point in the sequence of integration steps.

Langevin dynamics-based samplers. Langevin dynamics samplers have been implemented in several variants, including Geometric Langevin Algorithm (GLA) with first and second order time integrators, see [8], and the second-order BAOAB method, see [46].

SGLD implementation. Discretized Brownian dynamics is available in the form of SGLD, see [71]. Within the *TensorFlow* framework³ “Probability” (TFP) [15] a preconditioned SGLD [51] optimizer is implemented intended for probabilistic reasoning and statistical analysis. It is also based on the `Optimizer` class. There, the same preconditioner as in RMSprop [30] is used as replacement to the

³<https://www.tensorflow.org/probability/>

intractable Fisher information. However, as it uses a preconditioning matrix, it is not directly comparable to our unpreconditioned scheme as its computational complexity is higher. A scheme with similar intent is available in TATi if SGLD is used together with the ensemble quasi-Newton (EQN) method. However, EQN does not estimate a diagonal matrix but calculates a low-rank approximation of the local covariance from an ensemble of walkers.

HMC implementation. Hamiltonian dynamics with Metropolis-Hastings is implemented in the form of HMC [58] based on Verlet time discretization. For the HMC method, based on *TensorFlow*’s `Optimizer` class, conditionals (“if” statements) are required to allow for branching in the program flow: Depending on the current step, either a leapfrog integration step is computed or the MH criterion is evaluated. The final step is accepted or not depending on a random number compared to the criterion (15)’s threshold value. In *TensorFlow* conditionals have the peculiarity that nodes in either branch are evaluated as others may depend on them. All side effects of each branch have to be hidden in a `control_dependencies` statement.

Due to initial force evaluation and the conditionals, the Hamiltonian dynamics sampler requires $l + 2$ gradient evaluations for computing l discrete Hamiltonian dynamics steps. With Hamiltonian dynamics the computation of exactly l Verlet integration steps between initial state and proposal state is essential. Moreover, as this integration sequence is restarted from every state, we cannot exploit a zero gradient assumption as with the Langevin samplers. Therefore, in the very first step only $B_{\varepsilon/2}A_\varepsilon$ is computed, followed by $l - 1$ steps evaluating $B_{\varepsilon/2}B_{\varepsilon/2}A_\varepsilon$ and a last step to compute $B_{\varepsilon/2}$. Overall, the Verlet sequence $(B_{\varepsilon/2}A_\varepsilonB_{\varepsilon/2})^l$ becomes $B_{\varepsilon/2}A_\varepsilon \cdot (B_{\varepsilon/2}B_{\varepsilon/2}A_\varepsilon)^{l-1} \cdot B_{\varepsilon/2}$. This accounts for $l + 1$ gradient evaluations, one additional step is required to evaluate the MH criterion.

As we noted in the introduction, *TensorFlow* has a recently introduced `Probability` module, within which the MCMC framework provides an HMC sampler. It is possible to use it for sampling neural network loss manifolds by providing the log probability density $-\beta L(\theta, D)$. This MCMC framework is not based upon the `Optimizer` class. Instead it uses *TensorFlow*’s autodifferentiation capability to obtain gradients and contains a loop to sample a given number of states at a time within the computational graph. Furthermore, in its HMC implementation a Verlet (leapfrog) integrator is added to the computational graph, a loop for the number of desired leapfrog steps, and also MH conditionals that accept or reject the proposed state. Therefore, this implementation computes a whole chain of states within the computational graph. In other words, a single call to `Session.run()` computes a predefined number of sampled states. While this approach allows for very good parallelization, it has the drawback that, in the context of incomplete gradient calculation, it constrains the dataset used within the call and does not allow for mini-batching, as *TensorFlow*’s `dataset` uses iterators that are implemented as so-called *stateful* operations. (These are executed only once per `run()` call. If only a single state is sampled per call, then the parallelization is no longer as good and becomes equivalent to the one seen with the `Optimizer` approach.) Naturally, the batch is still fixed within the number of Verlet integration steps.

Note that this constraint only becomes apparent in the context of treating the loss manifold as a log probability density. There, however, mini-batching is frequently employed to ease the overly demanding computational burden of very large datasets. For these reasons we have not based our samplers on the MCMC framework contained in the `Probability` module.

Finally, we observe that a naive HMC implementation using stochastic gradients leads to very low acceptance rates and likely calls for more efficient schemes such as Stochastic Gradient Hamiltonian Monte Carlo (SGHMC) [10] with an additional friction term or for the use of thermostats to dissipate the induced noise, see [48]. The combination of HMC apparatus with thermostat methods for noisy gradient remains for future work.

3.2 Rapid Prototyping

Having discussed the sampler implementations in TATi we briefly show how the user may easily implement his or her own (sampling) methods.

In Listing 2 we have implemented a GLA second order sampler using the `simulation` module. GLA2 consists of the following steps, see section 2 for notation:

1. $p_{k+1/2} = p_k - \frac{\varepsilon}{2} \nabla L(\theta_k),$
2. $\theta_{k+1} = \theta_k + \varepsilon p_{k+1/2},$
3. $\hat{p}_{k+1} = p_{k+1/2} - \frac{\varepsilon}{2} \nabla L(\theta_{k+1}),$
4. $p_{k+1} = \alpha \hat{p}_{k+1} + \sqrt{\beta^{-1}(1 - \alpha^2)} \cdot R_k.$

Listing 2: Example implementation of GLA 2nd order using the `simulation` module of TATi. Here, `gla2_update_step` performs the update step and `nn` instantiates the interface containing the neural network with a single node in the hidden layer. Finally, we perform 100 update steps and print the loss using `nn.loss()` and the set of parameters as `numpy` array through `nn.parameters()`.

```

import math
import numpy as np
import TATi.simulation as tati

def gla2_update_step(nn, momenta, old_gradients, step_width, beta, gamma):
    # 1. momentum integration
    momenta -= .5*step_width * old_gradients

    # 2. position integration
    nn.parameters = nn.parameters + step_width * momenta

    # 3. gradient evaluation and momentum integration
    gradients = nn.gradients()
    momenta -= .5*step_width * gradients

    # 4. random noise realization
    alpha = math.exp(-gamma*step_width)
    momenta = alpha * momenta + \
        math.sqrt((1.-math.pow(alpha,2.))/beta) * np.random.standard_normal(momenta.shape)

    return gradients, momenta

# instantiate interface class with network
nn = tati(
    batch_data_files=["dataset.tfrecord"],
    hidden_dimension=[1],
    seed=1,
)

# set up parameters and some variables
gamma = 10
beta = 1e3
momenta = np.zeros((nn.num_parameters()))
old_gradients = np.zeros((nn.num_parameters()))

# perform 100 sampling steps
for i in range(100):
    old_gradients, momenta = gla2_update_step(
        nn, momenta, old_gradients, step_width=1e-1, beta=beta, gamma=gamma)
    print("Step #"+str(i)+": "+str(nn.loss())+" at " \
        +str(nn.parameters())+", gradients "+str(old_gradients))

```

We define an update function `gla2_update_step` that uses `nn.gradients()` to get the gradients as a `numpy` array and that performs the steps $B_{\varepsilon/2}A_{\varepsilon}B_{\varepsilon/2}O_{\varepsilon}$. The interface class `simulation`, here nicknamed `tati`, constructs the network and prepares the input pipeline on instantiation. With a chosen set of parameters we sample for 100 steps and print the loss using `nn.loss()` at each step and also the network’s parameter using `nn.parameters()` (again as a `numpy` array) of which there are `nn.num_parameters()` many. Note that in this case the gradient evaluation using `nn.gradients()` is not constrained to occur at the beginning. Moreover, TATi makes sure (through caching) that loss and gradient are evaluated on the same batch despite occurring in different function calls, and that they match also with the returned parameters.

Naturally, this high-level interface has the drawback that the network’s parameters and gradients possibly need to be copied to and back from `numpy` arrays. We claim, however, that for medium-sized networks and datasets a factor of 10 increase in runtime is acceptable for a rapid prototype that can later be used to test a full implementation against.

3.3 Ensemble Methods

Ensemble methods in machine learning such as random forests or boosting (see [73] for an overview and applications) are used to decrease bias and improve predictions.

Here, we look at enhanced ensemble methods where trajectories are sampled in parallel and between which information may be exchanged for the benefit of improved exploration, increased speed, decreased bias and other reasons, see [56].

For designing such ensemble methods, two approaches are possible:

- the parallelization may be done with different processes where each process owns a unique *TensorFlow* `Session` object, or
- the network as a whole has to be replicated and used within the same `Session` object.

Both approaches have been implemented in TATi.

Using the second approach it is easily possible to exchange information during sampling between different walkers. By *walker* we designate an individual set of network parameters that is modified over time through dynamics. *TensorFlow*’s concept of namespaces helps to properly separate nodes of identical functionality associated to a unique walker from others.

Process-wise parallelization is done in *TATiExplorer* where, for example, a diffusion map-based exploration scheme has been implemented to enhance the discovery of the loss landscape; full testing and evaluation of this scheme remains for future work.

Thread-wise parallelization by using *TensorFlow*'s inherent means of executing nodes in the computational graph in parallel is also contained in TATi. It is activated simply by specifying TATi's parameter `number_walkers` larger than 1. In this case, the neural network with all degrees of freedom and the sampler method is replicated, once per walker. If the sampling step node is evaluated, all walkers perform a single, independent sampling step in parallel, reading the same batch of the dataset, but each with distinct injected random noise process if required.

In order to highlight the usefulness of the ensemble methods, we have used the thread-based approach to implement an ensemble quasi-Newton-scheme where the walkers exchange information about their position for a local approximation of the covariance matrix. This information can be used to compute a preconditioning matrix for faster exploration, see section 2 for details.

4 Software Performance Results

In this section, we quantify the runtime performance of the software. To this end, we look at TATi's input pipeline and compare sampler runtimes against the GD optimizer runtime. Moreover, we will be comparing runtimes on CPU-only as well as GPU-assisted systems.

All of the following performance measurements have been executed on "DS5 v2" (Intel(R) Xeon(R) CPU E5-2673 v4 @ 2.30 GHz, 16 virtual cores, 56 Gb memory) and "NC12s v3" (Intel(R) Xeon(R) CPU E5-2690 v4 @ 2.60 GHz, 12 virtual cores, 224 Gb) instances in the Microsoft Azure cloud. The latter type has two NVIDIA Tesla V100 GPU cards with 16 Gb memory installed that are utilized by *TensorFlow*. At any given time only a single process was run to maximize parallel execution.

All experiments were done using *TensorFlow* version 1.4.1 but tests showed equivalent performance up to version 1.12.⁴ Moreover, we have used TATi version 0.9.2.

In order to test the throughput in all of the following experiments, we look at the runtime, averaged⁵ over 10 consecutive steps, for 1,000 steps in total. The perceptron employed has up to a single hidden layer with the number of nodes picked from $\{0, 10, 100, 1000\}$. We mimicked the MNIST dataset by using 784 features and 10 labels with each drawn at random. We pick the number of items, i.e. the dimension of the dataset, from $\{500, 1600, 5000, 16000\}$. These datasets are stored as simple CSV files as they are comparatively small. Moreover, we look at various batch sizes in 100, 1000, 10000. Note when the batch size exceeds the dataset dimension, it is capped. We sample from an equilibrated position to avoid numerical instabilities. We use 3 sampling runs with different random number generator seeds to obtain average and rough estimates of the standard deviation.

4.1 Input Pipeline

The first performance-critical component we look at consists of the two input pipelines. TATi contains one pipeline based on *TensorFlow*'s `dataset` module where nodes are added to the computational graph that parse files and preprocess the data such as to match with the input and output layer dimensions and types. This causes the dataset files to be read in parts when the evaluation of these nodes in the graph is triggered. The module comes with a cache functionality such that expensive manipulations do not need to be re-done after the first epoch. We have made use of `map`, `interleave`, `cache`, and `prefetch` mechanisms in the implementation and tested it extensively for maximum performance⁶.

The second pipeline uses `numpy` arrays that can be fed into the network through *TensorFlow*'s `feed_dict` mechanism. This is referred to as *in-memory pipeline*. The parsing is done prior to any sampling steps. Note that *TensorFlow* disapproves this mechanism for extensive data sets for performance reasons. However, as we will show, it is feasible for datasets at least up to a size comparable to that of MNIST.

In Figure 3(a) we show the run time per 10 steps over the 1,000 samples steps, once for the in-memory pipeline and once for the dataset pipeline for various batch sizes. We picked a random dataset of 5,000 items and BAOAB as sampler with step size of $1 \cdot 10^{-1}$. The other dataset sizes yield comparable results.

We observe that the dataset pipeline curve has a spike that is directly connected to initial reading of the dataset files into memory. After one epoch has passed, e.g., 50 steps for the smallest of the chosen batch sizes, the whole file has been read into memory and is cached. We see that the run time nonetheless favors the in-memory pipeline for small batch sizes. The dataset pipeline is faster for large batch sizes.

⁴Newer *TensorFlow* versions are supported once they become available within *Anaconda*, <https://www.anaconda.com/>.

⁵This is to average out effects such as harddrive access.

⁶Taking into account hints in *TensorFlow*'s performance guide and evaluating their use on the given dataset.

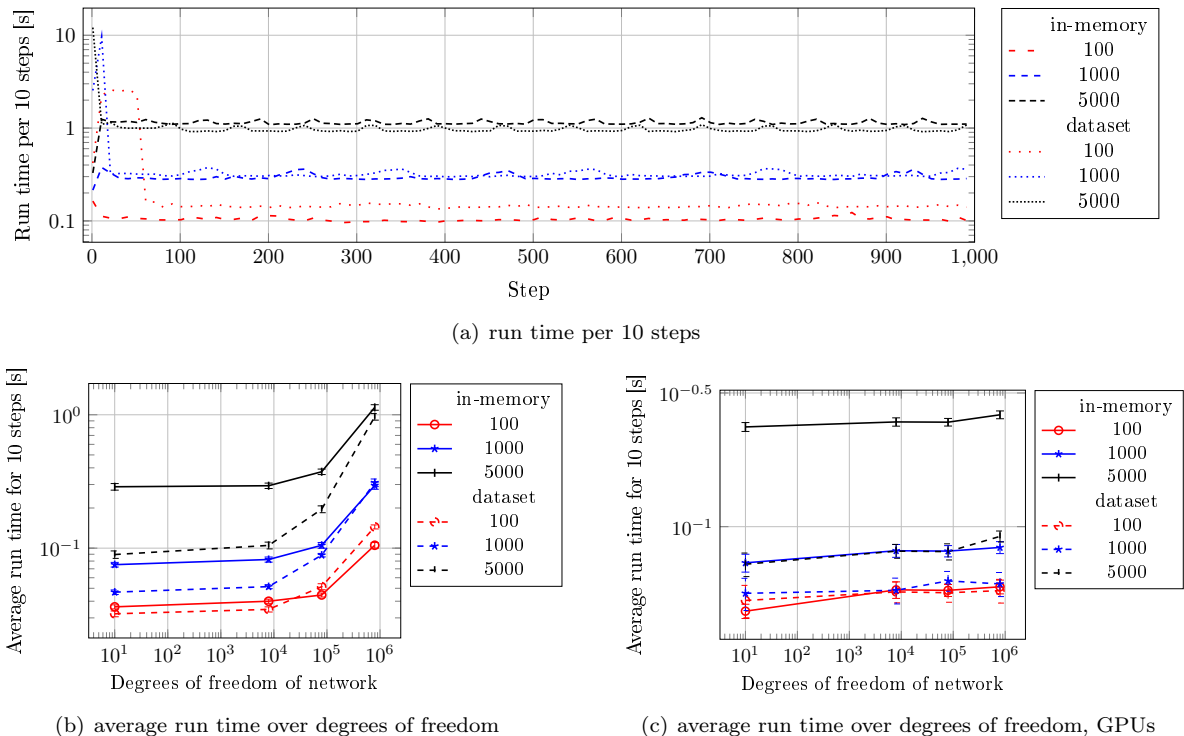


Figure 3: Comparison of the in-memory (solid) and the dataset (dashed) pipeline for an multi-layer perceptron with about 10^6 dof and a fixed dataset of size 5,000 over different batch sizes (see legend). (a) Run time per 10 steps over the 1,000 sampled steps using BAOAB. (b), (c) Average run time per 10 steps over the degrees of freedom of the network on CPU only and GPU-assisted hardware, extracted from averaging over steps 500 to 1,000 in (a) Both pipelines are seen to have their merits in different regimes of network and batch size.

In Figure 3(b) we take a closer look and plot the average runtime over the number of degrees of freedom of the network, extracted from step 500 till 1,000 in Figure 3(a) to avoid the initial loading.

There we see that the dataset pipeline is generally faster for smaller networks. For larger networks, there is always a cross-over point where the in-memory pipeline takes over. This is different on GPU-assisted hardware. There, for larger batch sizes the dataset pipeline is always faster, the difference depending on the exact batch size, see Figure 3(c). We note that the picture was unchanged for more items in the dataset.

We further observe that the parallel load of the system is typically greater by a factor of 2 or 3 with the dataset pipeline than with the in-memory pipeline although there is no equally strong difference in run time. This might explain why for large networks the in-memory pipeline is faster: the measured runtime comes from a balance between the parallelization needs of two tasks, memory copying and linear algebra. With larger networks the latter requires more time and threads. Hence, fewer threads are available for the dataset pipeline which then takes longer overall.

All in all, we note that both pipelines have their merits: On CPU-only/shared-memory systems for large networks, the in-memory pipeline is advised if the dataset fits in memory as it is slightly faster and has a smaller load. For GPU-assisted systems the dataset pipeline is generally preferred.

4.2 Optimizer vs. Samplers

In determining the runtime performance of our sampler implementations, we are bound by the performance delivered by *TensorFlow* itself. Therefore, we initially consider the optimization using its Gradient Descent (GD) implementation as the runtime baseline. In the GD update step (3), gradients are calculated, scaled by the learning rate and then used to modify the neural network’s parameters. This has been implemented in *TensorFlow* using kernel functions written in C++.

All samplers that we have additionally implemented using *TensorFlow*’s *Python* API require more operations such as evaluating a random noise tensor and additional matrix multiplications, see Table 2 for a summary.

We next outline how to measure the sampler runtime and explain what to compare in order to properly assess the additional cost when sampling. In order to offer both ease-of-use and flexibility in

incorporating various sampling methods, an extra layer of abstraction is added to TATi that incurs an additional runtime cost. This penalty due to the extra abstraction compared to a pure *TensorFlow*'s GD implementation is about 10-15% measured on the network and dataset setup discussed at the section start.

Moreover, TATi also does some additional bookkeeping of kinetic and potential energies, of the norms of momentum, gradient, noise, and other values that incur extra costs due to scalar multiplications. Note that these “book-keeping” calculations cost about 20-25% in runtime performance, but they may be switched off entirely when not required for sampler operation.

Therefore, we compare the extended GD implementation in TATi to the other samplers to properly assess the performance penalty. In this setting, the difference in runtime is caused only by any additional operations of samplers compared to the GD update step.

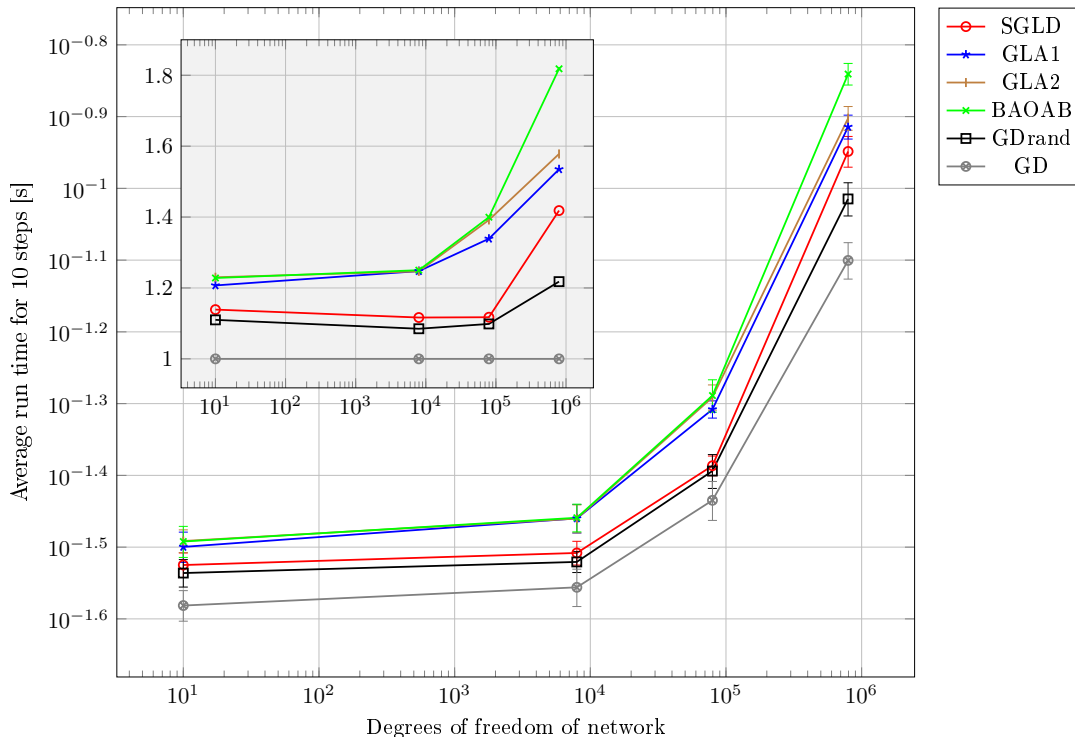


Figure 4: Comparison of the runtime per 10 steps over all Langevin samplers (see text), GD as optimizer and GD with an artificial random noise tensor evaluation added (GDrand). The inset shows the runtimes relative to that of GD. A maximum factor of 1.8 for BAOAB is a very modest increase, compared to SGLD we only have around 20% extra runtime.

In Figure 4 we look at the average run time required for 10 consecutive steps in relation to the number of degrees of freedom of the network. Note that the latter depends on n the number of hidden nodes by $n + 10 + (784 + 10)n$ for the chosen multi-layer perceptron with a single hidden layer. We use a batch size of 100, a dataset size of 5,000 items, and the dataset input pipeline.

Overall, the largest runtime increase is a factor of 1.8 between GD and BAOAB for the largest network. Up to a factor of 6 could be expected if the computation of the gradient itself is neglected, see Table 2. Naturally, all samplers require more run time in general than GD as they involve additional operations. However, the overall increase in run time is in comparison very moderate. The cost of the gradient computation alone seems to dominate.

Note that we have added runtimes for a GD variant where an additional random number tensor is evaluated that does not affect the optimization itself. This is to highlight the extra cost of the random number term that is also contained in Stochastic Gradient Langevin Dynamics (SGLD). We see that the random number evaluation requires about an order of magnitude less time than the linear algebra computations.

Hence, we conclude that sampling compared to optimization is not very costly. More important, sampling more accurately, by choosing GLA2 or better BAOAB over SGLD, just incurs extra run time of around 10% to 20%.

Table 2: Computational complexity required for each building block (top) and therefore in turn for each optimizer and Langevin dynamics sampler implemented in TATi (bottom). Each block has a complexity of $\mathcal{O}(N)$ with N the number of degrees of freedom but different scaling constants. One could expect a cost penalty factor for BAOAB compared to GD of up to 6. Similarly, a factor of up to 3 compared to SGLD.

block/sampler	scalar multiplication	addition	assignment	random tensor
A	1	1	0	0
B	1	1	0	0
O	2	1	1	1
GD	1	1	0	0
GD rand	1	1	0	1
SGLD	2	2	0	1
GLA 1	4	3	1	1
GLA 2	5	4	1	1
BAOAB	6	5	1	1

4.3 Performance on GPUs

As a last step, we would like to highlight the performance when using special purpose hardware in the form of Graphic Processing Units (GPUs) that are especially tuned for linear matrix algebra operations such as matrix multiplication and summation.

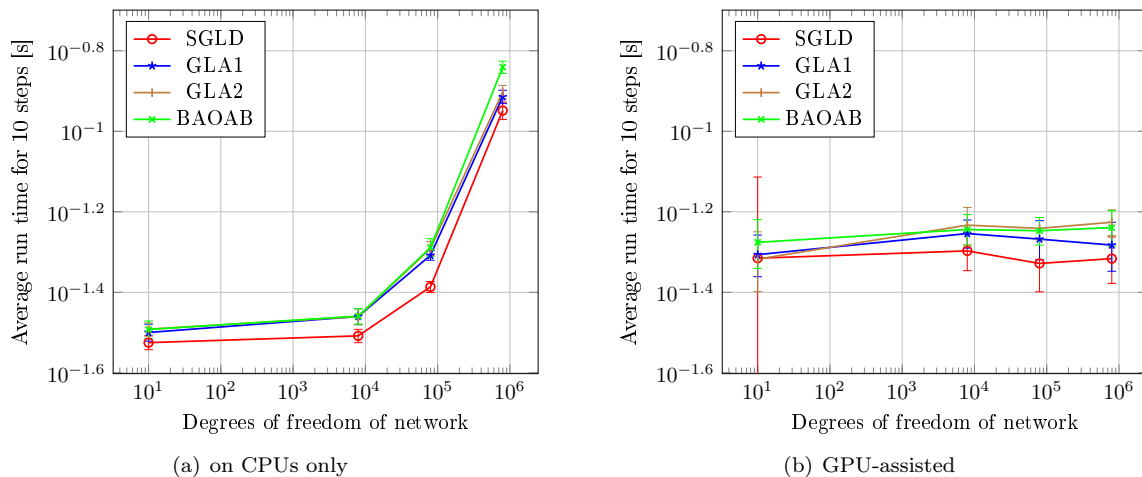


Figure 5: Comparison of the averaged runtime per 10 steps, extracted between step 500 and step 1,000, c.f. Figure 3(a), over all samplers on CPU-only and GPU-assisted hardware. Both plots have the same fixed y scale. For small networks there is noticeable overhead for GPU-assisted hardware. For the larger networks investigated here there is (almost) perfect scaling with increased degrees of freedom.

In Figure 5 we compare the average run time per 10 sampling steps over the degrees of freedom of the multi-layer perceptron for CPU-only and GPU-assisted hardware configurations over the samplers only. Again, we use a batch size of 100, a dataset size of 5,000 items, and the dataset input pipeline.

We see that the runtime increases distinctly for increasing degrees of freedom of the network when a CPU-only system is employed. In contrast, the system that contains additional GPU hardware sees no increase in the runtime for the investigated degrees of freedom. We remark, without showing, that for a batch size of 10,000 an increase is visible in the last data point associated with about 10⁶ degrees of freedom.

However, for small-sized networks up to 10⁵ degrees of freedom the GPU-assisted hardware is actually slower, probably due to additional copy operations from CPU to GPU memory.

4.4 HMC comparison

As mentioned in section 3.1, there is also an HMC implementation within *TensorFlow*'s Probability (TFP) module. We briefly compare this implementation in the scope of sampling loss manifolds against the one in TATi.

The scope of the TFP implementation is general, allowing to sample from arbitrary log posterior distributions. Hence, we first need to build a neural network depending on parameters θ where we then sample $-\beta L(\theta, \mathcal{D})$. Its loss $L(\theta, \mathcal{D})$ depends on the dataset where we tested two variants on feeding it into the network: In the first variant, the `dataset`'s iterator nodes are directly taken as the input layer and as the labels in the loss function. Then, only a single `Session.run()` call (without a `feed_dict`) is needed to execute the sampling step(s). In the second variant, `placeholders` are used for the input layer and the labels. The next batch is obtained in an extra `Session.run()` call and placed in a `feed_dict` given to the second call that executes the HMC sampling step.

The TFP framework allows to sample multiple MCMC states per `Session.run()` call, we detailed its restrictions in section 3.1. This fixes the current dataset batch throughout these samples states which is not the case for TATi's HMC. Therefore, in either of the TFP implementation variants we have enforced sampling of a single state per call to allow for comparison against TATi's HMC implementation on an equal basis.

For TATi we use *TATiSampler* with the in-memory pipeline as it is closest to the approach used by the TFP variants.

We are interested in the runtime performance for a single-layer perceptron with an MNIST-like random datasets, having 784 input features, 10 output classes with 1,000 datums in total.

For brevity we just mention the results without figures: Note that all three implementations show a broadly similar parallel load. The load for both TFP variants is higher by a few tens of percents. This could be explained by the extra layer of abstraction present in TATi. We notice that the HMC in *TATiSampler* is slower by a constant factor of 3 if we compare against the TFP implementation based on placeholders. However, this needs to be contrasted with the fact that TATi requires $2 \cdot (l + 2)$ calls to `Session.run()` while TFP only needs 2 calls in total, independent of the number of leapfrog steps l . This is a fundamental difference as TATi's samplers are based on the `Optimizer` class while TFP encodes the sampling loop from scratch in its MCMC framework. Again, we mention that the latter approach is not well-suited to support mini-batching.

Despite the possible need to copy the next batch into the `feed_dict` the placeholder variant is faster than the variant where the `dataset`'s iterator have been coupled directly. Obviously, the copying is avoided by using references to memory locations instead. Both variants become equivalent in runtime only for large number of leapfrog steps (>10).

5 Numerical Experiments

In this section, we perform numerical experiments to study the convergence rates of the samplers implemented in TATi for the simplified case of a harmonic oscillator, comparing them with analytically known rates. Next, we use the MNIST dataset on a single-layer perceptron to illustrate an enhanced loss landscape visualization technique that obtains its projection directions from sampling trajectories. Finally, we present results on the EQN method described in Section 2 for a Gaussian model and for a single (internal) layer perceptron applied to the MNIST dataset.

5.1 Sampler Properties and Error Analysis

In this error analysis, we explore a state $\{\theta, p\}$ with position θ and momentum p of a single degree of freedom. The kinetic energy is defined as $\varphi(\theta, p) = \frac{1}{2}p^T p$, where we have set the mass matrix to unity. Its asymptotic value in the canonical distribution is given by the number of parameters N and the (inverse) temperature β as $\frac{1}{2\beta}$, see [46, sect. 6.1.5]. The virial is defined as $\varphi(\theta, p) = \sum_i^N \theta_i \cdot \nabla_i L(\theta) = \theta \cdot \nabla L(\theta)$, where $\nabla_i L(\theta)$ is the derivative of the loss function with respect to the parameter θ_i . Its asymptotic value is two times that of the kinetic energy, as a consequence of the virial theorem. For this theorem to hold we need a potential that is unbounded from above and grows sufficiently rapidly at infinity, see appendix A.1 for a derivation.

Averages of the kinetic energy or of the virial are examples of time integrals of (7) that can be used to assess the accuracy of the chosen dynamics and discretization, since their asymptotic values are known. As we are interested in discretized integrals over finite number of time steps, which are accessible in numerical computations in the absence of analytical solutions, we look at estimators (14) of the following form

$$\hat{\varphi}_N = \frac{1}{N} \sum_{n=0}^{N-1} \varphi(q_n, p_n).$$

The total error with respect to the expected value $E_\mu(\varphi)$ for the invariant probability measure μ decomposes as

$$E(|\hat{\varphi}_N - E_\mu(\varphi)|^2) = (E(\hat{\varphi}_N) - E_\mu(\varphi))^2 + E(|\hat{\varphi}_N - E(\hat{\varphi}_N)|^2), \quad (20)$$

i.e. it is a combination of the *discretization error*, from the finite step size when discretizing the dynamics (9), and the *sampling error* that results from the inability to sample over an infinite time or to generate an infinite number of steps. The first source is also sometimes referred to as the perfect sampling bias, emphasizing its presence even in the limit of infinitely many samples.

In the extreme case of a vanishing gradient, only the sampling error is present. This error will decay so that its variance is proportional to $1/N$. A more interesting case is that of a “harmonic potential” $I(\theta) = a\theta^2/2$, in which case the truncation error is nontrivial.

5.1.1 Truncation Error for Harmonic Potential

We have contributions to the total error (20) from both the sampling error and the discretization error. We will see that the latter may dominate when the scale a of the potential and therefore the average gradients are sufficiently large. We concentrate here on the empirical results as we aim to verify the sampler implementation in TATi, see [46, sect. 7.4] for a general discussion of harmonic problems in the context of Langevin dynamics. We use a single-layer perceptron with a single input node and a single output node with linear activation and zero bias, i.e. $f_\theta(x_i) = \theta_1 x_i$. We use the mean squared loss function. Then, such a harmonic potential can be easily introduced by a dataset with the square root of the prefactor as its single feature and a zero label, i.e. the only dataset item is $(X, Y) = (\sqrt{a}, 0)$. We use three different factors $a \in \{0.01, 1, 4\}$. Moreover, we use the same sets of parameters for γ , β , and ε as before. Here, we employ BAOAB as the sampler, again with 10^6 sampling steps.

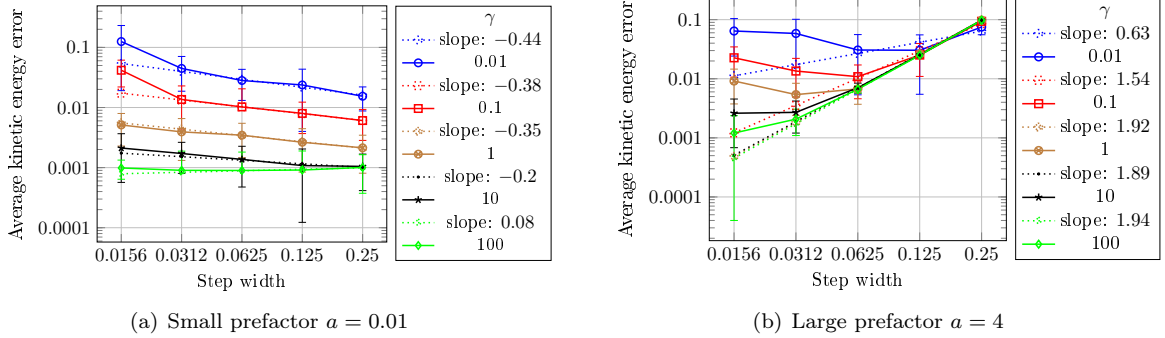


Figure 6: Highlighting the truncation error with respect to the step size by showing the relative error of the average kinetic energy with respect to its asymptotic value for the “quadratic potential” case. (a) If the gradients are small, the system performs a pure random walk and results are independent of stepsize. (b) Given large enough gradients relative to the temperature the convergence order of the integration method with the step size becomes apparent, here second order for BAOAB in the momenta.

Examining Figure 6(a) where we use a small prefactor a , we notice that the error decreases with increasing step size because α becomes smaller and therefore we obtain more random walk-like behavior. However, it does not entirely depend solely on α , but also to some extent on the step size ε . For the highest value of $\gamma = 100$ we again have a flat line due to the lower bound enforced by the CLT.

In Figure 6(b) with a large prefactor a we notice that for large step sizes all of the curves coincide regardless of γ and the behavior has reversed: now the error becomes smaller for smaller step sizes. Naturally, the reason for this change is the discretization error that arises because of substantial non-zero gradients, and that the error depends on the step size ε . Measuring the slope in the domain where all curves overlap for $a = 4$, we obtain values of up to 2, i.e. second order convergence in the discretization error as expected from BAOAB. In place of the prefactor a we could also have varied the inverse temperature β to the same effect that only depends on the scale of the noise relative to the scale of the gradients.

Using a higher-order sampler allows for a smaller error at a given step size or to use larger step sizes (and therefore sample more space) for a given error threshold. Note that the step size is bounded from above by a stability threshold. The benefit of the trade-off between accuracy and computational effort is limited however, and it is likely that very high order schemes (beyond the second order splittings discussed here) are not efficacious in TATi, in keeping with previous studies in molecular dynamics [47].

For comparison, we also look at the average virials in Figure 7. However, they depend only on the position and *not* on momentum. Note that the BAOAB scheme has nil perfect sampling bias for purely configurational quantities such as virials. Here, we are instead using the GLA 2nd order sampler but keep all the other aspects of the method unchanged.

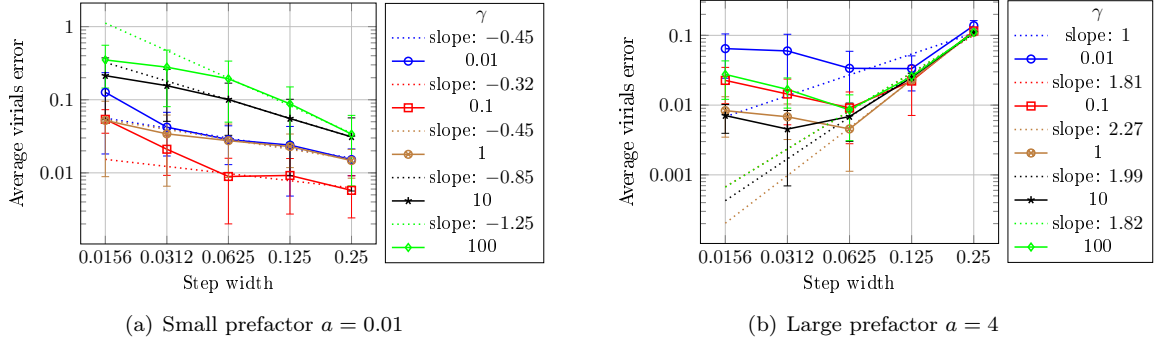


Figure 7: Relative error of the average virial with respect to its asymptotic value for the “quadratic potential” case using GLA2 sampler. Again, we see second order convergence, here in the positions, given the gradients are large enough relative to the noise, see also Figure 6.

We obtain the same qualitative picture for the average virials sampling with GLA2 as we got with the average kinetic energy sampling with BAOAB. Again, for a large enough prefactor the discretization error dominates. Inspecting the slopes in the doubly logarithmic plots, we find values around 2 that peak for $\gamma = 1$.

5.1.2 Langevin Sampler Performance in a Two-Cluster Classification Problem

In the following we will be inspecting the average virial, obtained over sampled, finite trajectories in order to assess the accuracies of positions obtained from various samplers. We will be investigating the following samplers: Stochastic Gradient Langevin Dynamics (SGLD), Geometric Langevin Algorithm (GLA) 1st and 2nd order, and BAOAB.

Very long runs are needed to bring forth the different convergence order of the discretization error because of the involved statistical errors. Therefore, we still use a very simple dataset: it consists of 500 points drawn from two Gaussians in two dimensions, one centered at $[2, 2]$ with label 1, the other centered at $[-2, -2]$ with label -1 . The points are additionally perturbed by 0.1 relative noise.

We use a single-layer perceptron with two input nodes, a single output node with linear activation and mean squared loss. Therefore, the network has $N = 3$ parameters in total, two weight degrees and one bias degree.

The parameters are first equilibrated for 2,000 steps with a learning rate of 0.03 with Gradient Descent (GD). Next, we perform sampling runs from the resulting position for 10^6 steps at various step sizes. In the case of a sampler based on Langevin dynamics, we use a friction constant $\gamma = 10$ and an inverse temperature $\beta = 10$. Note that, because we start at an equilibrated position with zero gradients and because the potential function is squared, positions are only rescaled when using other temperatures if the same random number sequence is used. We use 100 different seeds and average the last average value per trajectory over all seeds.

In Figure 8 we give the absolute error between the average virial and its asymptotic value scaled by the inverse temperature β per sampler for each step size employed. Note again that the virial depends on the positions and the gradient. Moreover, we remark that increasing the largest step size shown for each sampler individually by a factor of two would cause the dynamics to become unstable. Naturally, the exact threshold depends on the magnitude of the gradients and therefore on the dataset.

The slopes have been obtained from least squares regression fits where the data point to the smallest step size have been weighted by $\frac{1}{10}$.

We make the following observations: GLA2 has second order convergence in the average virial, GLA1 has first-order convergence. BAOAB shows such great accuracy at this finite trajectory length that its second to fourth order convergence does not show as it reaches the CLT limit. These results are in absolute agreement with results from an analysis on harmonic problems, see [46, sect. 7.4.1]. Note that SGLD exhibits second-order convergence in the virial in this example; actually this is an artifact of the way the data has been graphed: the SGLD ‘step size’ can be viewed as the square root of the step size

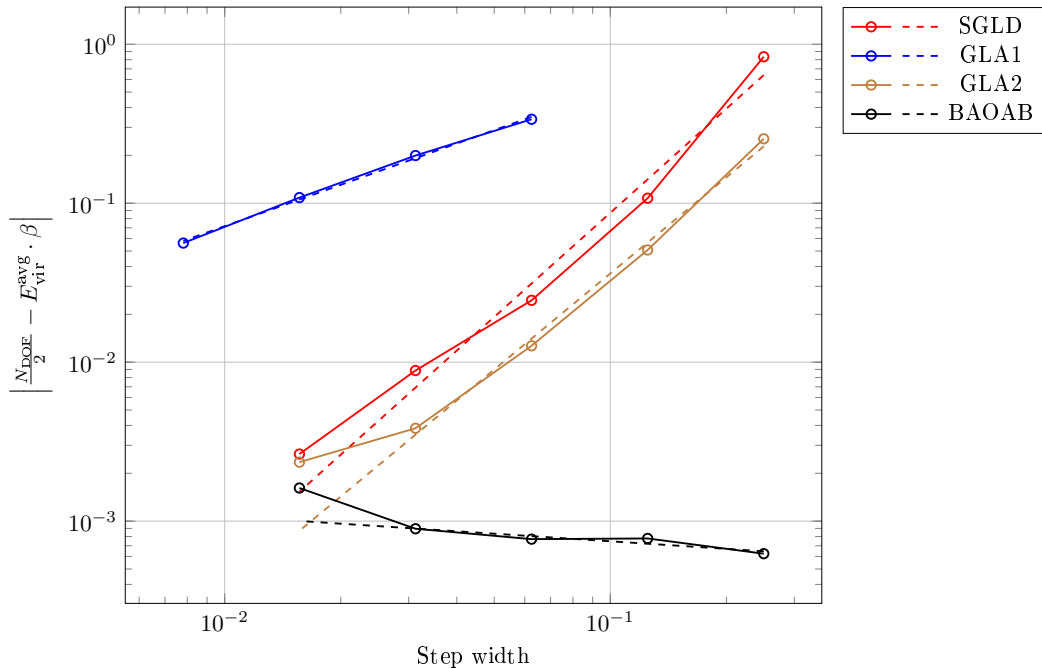


Figure 8: Order of convergence for the discretization error for four samplers of the average average virial for the simple two clusters dataset. Dynamics become unstable if the largest step sizes are increased by a factor of two. GLA1 has first order (slope 0.86). SGLD (slope 2.18) and GLA2 (slope 2.01) have second order. BAOAB’s accuracy on the position marginal is so good that its second to fourth order convergence cannot be seen against the lower bound of the CLT.

$\sqrt{\varepsilon}$ of the other samplers, see [46, p. 36], i.e. it is really a first order scheme when expressed in the standard way.

From these results the sampling method of choice seems to be BAOAB which has superior accuracy in the positions and general second order convergence at little computational overhead and extra memory requirement, compared to SGLD. Note that SGLD is based on Brownian dynamics, thus lacking momenta, and therefore is expected to be less efficient in exploration for multimodal problems than BAOAB or other Langevin dynamics samplers [47].

A similar study on the MNIST dataset is impeded by its wide-spread covariance eigenvalue spectrum, shown in the next section. There we encounter both large and small gradients and therefore have a mixture of the “flat potential” and “harmonic potential” cases which obscures the convergence orders. However, choosing a high-accuracy integration method is nonetheless very important there as well, as the presence of large gradients (or large directional derivatives) will dominate the exploration.

5.2 Application: Loss Manifold Analysis for MNIST dataset

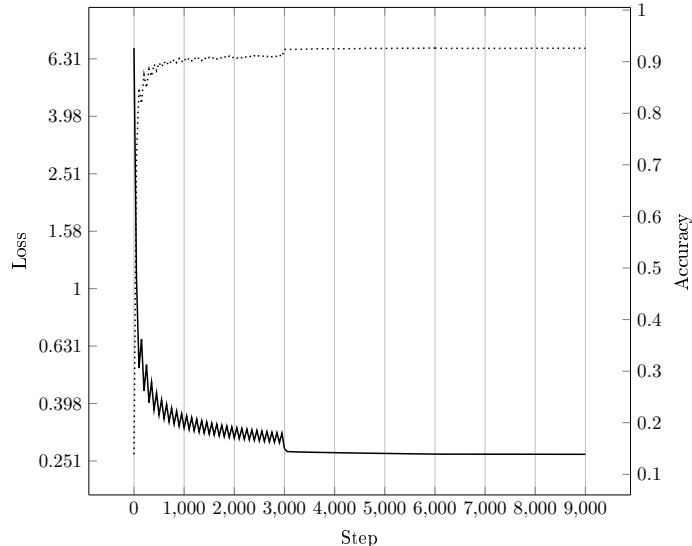
We now turn to a somewhat more elaborate setting: The MNIST training data set consisting of handwritten digits (zero to nine) in 70,000 grey-scale images of 28x28 pixels, see [41]. We have split off a validation set of 10,000 images that is left aside. The remaining 60,000 images are split again into a test set of 5,000 images and a training data set of 55,000 images.

The simplest network to tackle this classification problem is again a single-layer perceptron with 784 input nodes and 10 output nodes. We use linear output activation and the softmax cross-entropy as loss function. The accuracy is quantified by the strongest output (argmax).

We first employ SGD as optimizer with a batch size of 550 for 9000 steps and an initial learning rate of 0.5 that is reduced to 0.05 while the batch size is increased to 5,500 after 3,000 steps and finally down to 0.01 with no more mini-batching after 6,000 steps. We obtain a loss of 0.265 and 92.6% accuracy on the training dataset and a loss of 0.271 and 92.6% accuracy on the test dataset, c.f. 91.6% and 92.4% in [43].

The resulting loss per step is given in Figure 9. There are oscillations due to the stochastic gradients that decrease with the learning rate and with the batch size.

In order to inspect the quality of the minimum found, we need to look at the resulting loss manifold around the minimum location. As the network has 7850 degrees of freedom in total, we need appropriate



(a) Loss (solid) and accuracy (dotted) along the optimization trajectory

Figure 9: Loss and accuracy values along the optimization trajectories consisting of three parts (blue, gray and black) where only every 10th step is shown. The optimization yields 92.6% test and training set accuracy.

techniques for its visualization. Several of these are discussed in [52]. In place of random directions, proposed in [23], that frequently only show little variation [52], we use directions associated with a. the largest eigenvalue, and b. a very small eigenvalue of the covariance matrix.

The covariance matrix is obtained from sampling runs of 10^6 steps using BAOAB with a step size $\varepsilon = 0.125$, $\gamma = 10$, $\beta = 10$, and a batch size of 550. Each of the three runs in total starts from the same position, equilibrated with SGD with the same batch size of 550, for 5000 steps with a learning rate of 0.5. However, each run uses a different random number seed and therefore will be subject to different temperature noise. Note that the specific initial position will not have an effect as the temperature is high enough to bring the walker quickly to a completely different position: see Figure 10(a) for loss values of all trajectories.

For obtaining the covariance matrix of very high-dimensional networks the trajectories from several (parallel) runs can be combined to overcome the computational burden. Moreover, a truncated eigendecomposition, e. g., using the power method and shift-and-invert, would fully suffice to obtain the largest and a small eigenvalue of a certain magnitude and their associated eigenvectors knowing that it is symmetric and positive semi-definite. The resulting eigenvalue spectra are given in Figure 10(b). Note that they are truncated to 1000 non-zero eigenvalues.

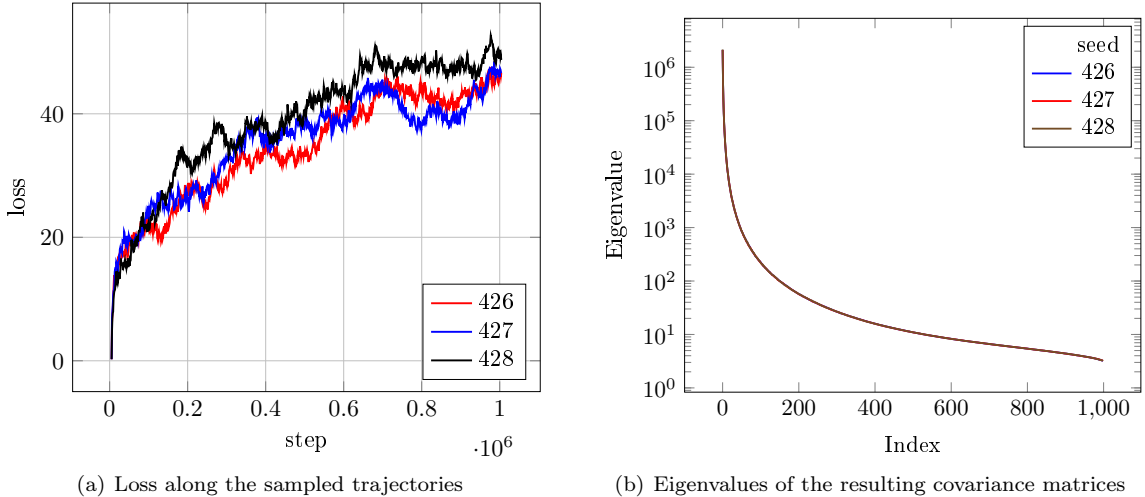
All three curves in Figure 10 coincide to a good degree in the logarithmic scale. The deviation is about 1%. This leads us to assume that the sampling runs have indeed been long enough. We expect that this eigenvalue spectrum shows the general covariance structure at large scale.

Observe that there is a strong decay of the eigenvalues' magnitude⁷. Therefore, we pick the first and 64th eigenvalues and use their associated eigenvectors as the directions v_1 and v_0 in which we plot the loss manifold.

Note that the strong decay indicates that random directions are hardly suited for the loss visualization (for MNIST) as on average these will not cover directions of strong covariance.

For visualizing the loss manifold, we sample it on an equidistant grid with 41 samples per axis along the two chosen directions $v_0 = (W_0, b_0)$, $v_1 = (W_1, b_1)$, split into weight components $W_j \in \mathbb{R}^{784 \times 10}$ and bias components $b_j \in \mathbb{R}^{10}$. We evaluate $\tilde{L}(c_0, c_1) = \sum_{i=1} \sigma(\tilde{f}(c_0, c_1), y_i)$ with the softmax cross-entropy σ and $\tilde{f}(c_0, c_1) = (W + c_0 W_0 + c_1 W_1) \cdot x + B + b_0 + b_1$, i. e. the loss constrained to the two-dimensional subspace and centered at the obtained (local) minimum at (W, B) . We use different intervals per axis of $[-10^i, 10^i]$ with $i \in \{1, 0, \dots, -4, -5\}$, endpoints included. For visualizing the previously obtained optimization trajectories, we re-evaluate them using the full training dataset (i. e. no mini-batches) per step and project them onto the two chosen directions. Note that also each sampled point of the loss manifold is evaluated using the full training dataset.

⁷One possible interpretation is that this decay resembles the Marchenko-Pastur distribution which describes the singular values of random matrices. However, we do not pursue this further in the scope of this article.



(a) Loss along the sampled trajectories

(b) Eigenvalues of the resulting covariance matrices

Figure 10: (a) Loss values along the sampled trajectories where only every 10th step is shown where trajectories obviously deviate rapidly from the initially same starting position. (b) Logarithmic depiction of the eigenvalues of the covariance matrix of three sampled trajectories. Each legend entry refers to the (different) random number seed employed. Spectra are in good agreement with about 1% deviation between the three random number seeds.

In Figure 11 we look at four of these manifold plots where we give the sampled manifold and the projected optimization trajectory. The x and y axis correspond to the two chosen directions, the z axis gives the loss as $\ln |\tilde{L}(c_0, c_1) - L_0|$, with respect to the lowest loss L_0 value found overall, at the specific point (c_0, c_1) in case of the sampled manifold and the true loss in case of the projected trajectory. Note that because of the projection the trajectory steps will not lie on the manifold itself.

In Figure 11(a) we recognize a large funnel where the c_0 direction is associated with the large eigenvalue and the c_1 direction is associated with the small eigenvalue. We see that the optimization trajectory gradually enters the funnel in (b). However, in (c) we realize that the previously obtained optimization trajectory ends prematurely, not in the possibly global minimum but stuck in one of the lower minima on the funnel wall in (d).

The intuition therefore is that the loss manifold resembles a large funnel whose extension though differs significantly in each direction. Its walls are dented with local minima, see Figure 12, especially at its bottom. Note that this funnel is not a product of the logarithmic scale, again see Figure 12 where a normal scale is used. This corresponds well with the observation in [23] that optimization runs never encounter serious obstacles and that there is a “sea of minima” in a small band of the loss bounded from below as proposed in [12] from translating results on spherical spin-glasses. Note though that the latter was derived for a different loss function.

This hints at the usefulness of second-order methods also for optimization, see [7] for a review.

Even in the limited scope of the two-dimensional projection we have seen that a minimum associated with an even smaller loss would have been attainable. However, the differences in the loss values are marginal, namely less than 10^{-5} . Naturally, this analysis is not complete. There are possibly multiple funnels from multiple minima with high barriers in between, as in the disconnectivity graphs by [1]. Recent work [17], however, suggests the contrary and corroborates our finding of a single funnel with many minima at its bottom. We conclude by remarking that this type of analysis can also easily be extended to multi-layer perceptrons and potentially to more advanced network architectures. Note that for multi-layer perceptron, scale invariance needs to be accounted for, see [52] for a normalization scheme.

5.3 Application: Ensemble quasi-Newton Method

As we have seen there is a large amount of anisotropy in the funnel observed in the loss manifold for the MNIST dataset. This results in huge variation in the projections of the gradient into different subspaces and is precisely the situation which motivated the development of the ensemble quasi-Newton scheme of Section 2.

TATi facilitates the implementation of a scheme such as the ensemble quasi-Newton method (see Section 2). Here we describe the implementation and investigate the method’s qualities in a simple, well understood model before returning to the MNIST dataset.

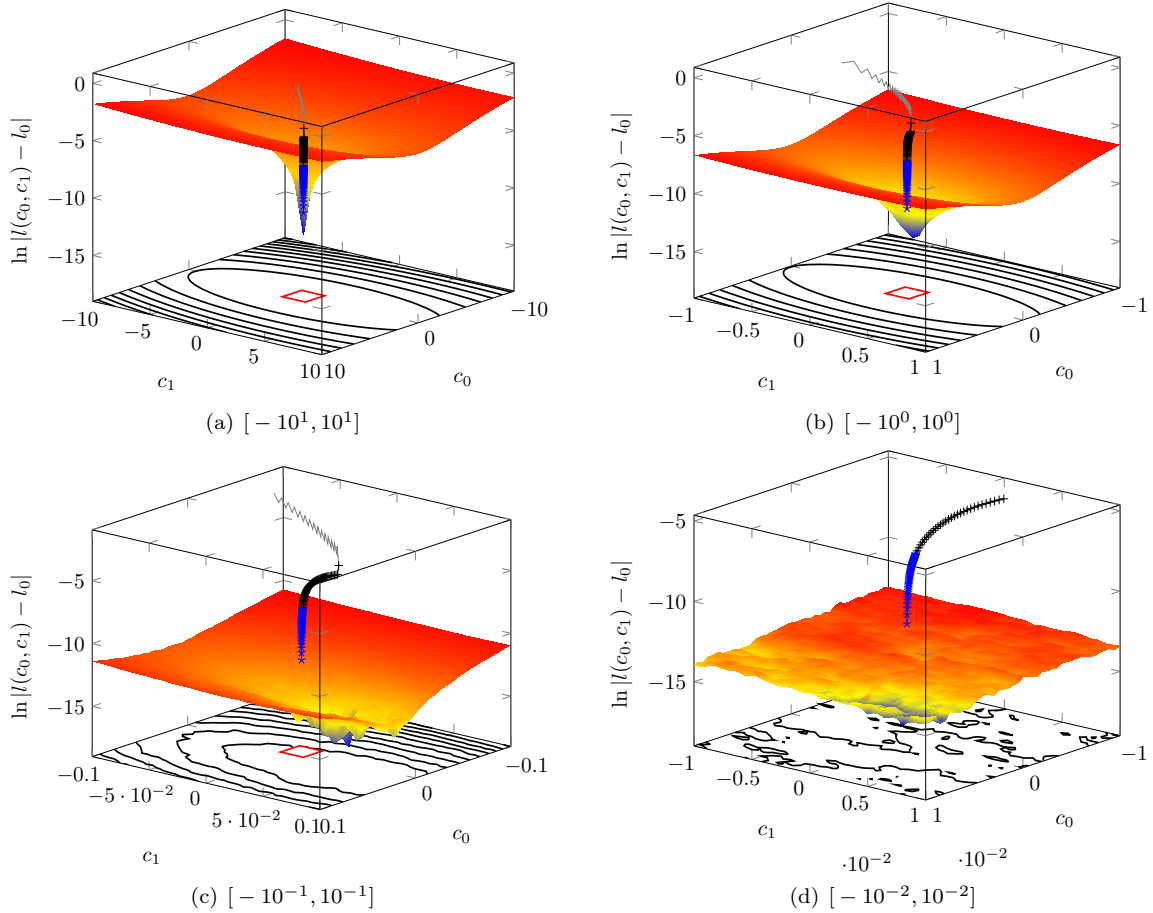


Figure 11: Visualization of the equidistantly sampled loss manifold for the MNIST dataset of single-layer perceptron with softmax cross-entropy loss function and linear activations. The two coordinate directions c_0 , c_1 correspond to the 1st and 64th eigenvalue (descending) of a covariance matrix sampled from a very long run. The z-axis, in *log scale*, corresponds to $\ln(\tilde{L}(c_0, c_1) - L_0)$, where L_0 is the smallest loss encountered overall. The value for z is also used to color the manifold. Additionally, an optimization trajectory using SGD consisting of three consecutive parts is given where after each leg the learning rate is reduced and batch size is increased. The terminal point of its last leg provides the point of origin. Only every 50th step is shown. Note that we show the exact loss for the whole training dataset for both manifold and trajectory. A red square shows the subsequent plot's domain.

5.3.1 Ensemble quasi-Newton

In Listing 3 we provide a rapid prototype of the algorithm using TATi's `simulation` module.

Listing 3: Example implementation of EQN using TATi's `simulation` module. We require for the number of walkers $L > 1$. We have skipped (...) the details of instantiation of the interface class `tati` setting the options.

```
import math
import numpy as np
import tensorflow
import TATi.simulation as tati

nn = tati(
    ....
)
options = nn.get_options()

def B(step_width, gradients):
    nonlocal momenta
    momenta -= .5 * step_width * np.dot( np.transpose(preconditioner), gradients)

def A(step_width, momenta):
    nn.parameters[walker_index] += .5 * step_width * preconditioner.dot(momenta)

def O(step_width, beta, gamma):
    nonlocal momenta
    alpha = math.exp(-gamma * step_width)
    momenta = alpha * momenta + \
        math.sqrt((1. - math.pow(alpha, 2.)) / beta) * np.random.standard_normal(momenta.shape)

B(step_width, old_gradients)
A(step_width, momenta)
O(step_width, beta, gamma)
A(step_width, momenta)
gradients = nn.gradients(walker_index=walker_index)
```

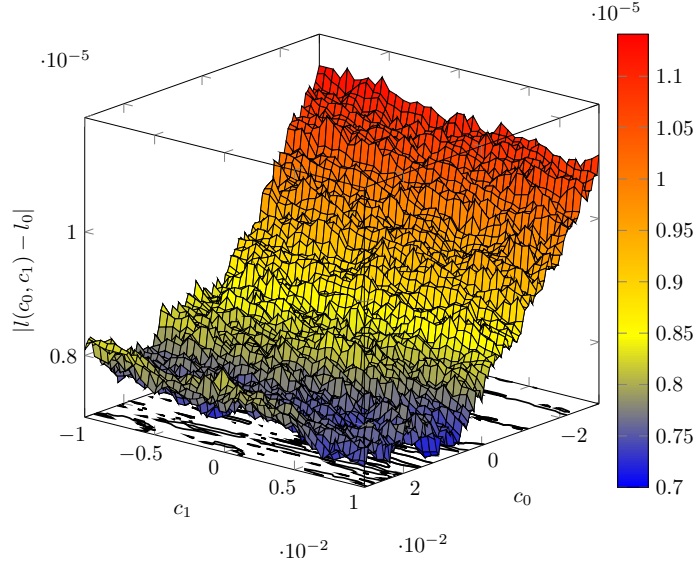


Figure 12: Sweep in the direction c_0 over five times the domain length with respect to Figure 11(d). The walls of the funnel’s bottom are dented with many local minima. Note that the figure is in linear scale for comparison to the log-scale before.

```

B(step_width, gradients)

return gradients, momenta

preconditioner = [np.identity((nn.num_parameters())) for i in range(options.number_walkers)]
normalization = 1./float(nn.num_walkers() - 1.)

def update_preconditioner():
    for walker_index in range(nn.num_walkers()):
        means = normalization*np.add.reduce([nn.parameters[i] for i in range(nn.num_walkers()) if i !=
            walker_index])
        covariance = normalization*np.add.reduce(\
            [np.outer(nn.parameters[i] - means, nn.parameters[i] - means) \
            for i in range(nn.num_walkers()) if i != walker_index])
        preconditioner[walker_index] = np.linalg.cholesky(\
            options.covariance_blending * covariance + np.identity((nn.num_parameters())))

momenta = [np.zeros((nn.num_parameters())) for i in range(options.number_walkers)]
old_gradients = [np.zeros((nn.num_parameters())) for i in range(options.number_walkers)]

def perform_step():
    for walker_index in range(nn.num_walkers()):
        old_gradients[walker_index], momenta[walker_index] = baoab_update_step(
            nn, momenta[walker_index], old_gradients[walker_index],
            preconditioner=preconditioner[walker_index],
            step_width=options.step_width,
            beta=options.inverse_temperature, gamma=options.friction_constant, walker_index=walker_index)

for step in range(options.max_steps):
    if (step) % options.covariance_after_steps:
        update_preconditioner()
    perform_step()

```

The full implementation with *TensorFlow* in TATi requires special care with the conditionals for the infrequent updates of B_i , needs to copy the network parameters to avoid changes within the parallel execution, and needs to compute the covariance matrices. All implemented samplers have been adapted in a similar way as in (18) to allow for preconditioning. For performance reasons the computation of $B_i^{(n)}$ could be done entirely through rank-1 updates.

5.3.2 Gaussian Model

A prototypical setting whose analytical properties are well-known is given by sampling from the Gaussian model,

$$\exp(-w^T C w) \quad (21)$$

with a covariance matrix $C \in \mathbb{R}^{n \times n}$. Here, we naturally encounter directions that are “slow” to sample, identified by large eigenvalues in C . In fact, when we (only) look at the covariance structure of the MNIST loss manifold, we replace it by an effective Gaussian model of that particular covariance matrix.

Transferring this model to the setting of sampling loss manifolds of neural networks is straightforward: We use the mean squared loss $l_\theta(f(\theta, x_i), y_i) = (f(\theta, x_i) - y_i)^2$ with the network’s prediction $f(\theta, x_i)$. Then, inserting into (2) in the case of n -dimensional input data $x_i \in \mathbb{R}^n$, single-dimensional output $y_i \in \mathbb{R}$, and a single-layer perceptron, i.e., $f_\theta(x) = w \cdot x + b$ with the parameters $\theta = \{w, b\}$ in the form of weights $w \in \mathbb{R}^n$ and of a bias $b \in \mathbb{R}$, we obtain

$$L(\theta, D) = \sum_i (w \cdot x_i + b - y_i)^2.$$

Setting the bias b and all outputs y_i to zero, we get

$$L(\theta, D) = \sum_i (w \cdot x_i)^2 = \sum_i \sum_{l,m=1}^n w_l(x_{l,i}x_{m,i})w_m = \sum_{l,m=1}^n w_l \left(\sum_i x_{l,i}x_{m,i} \right) w_m.$$

Note that we sample from the canonical Gibbs distribution $\exp(-\beta L(\theta, D))$. Therefore, the dataset needs to consist of rank-1 factors x_i that represent the chosen covariance matrix with components $C_{lm} = \sum_i x_{l,i}x_{m,i}$ in order to match this with (21). These factors can be obtained for example through an eigendecomposition $C = V\Lambda V^T$ as the eigenvectors V_i times the square root of their associated eigenvalue $\Lambda_{i,i}$. Naturally, any other (even non-orthogonal) decomposition into rank-1 factors would be admissible, too.

In order to produce random covariance matrices C of a certain structure, we resort to the following approach: We generate a random symmetric matrix, compute its eigendecomposition and modify the diagonal matrix D to consist of values picked from an equidistant spacing of the interval $[1, 100]$, where endpoints are included. This way we obtain a set of orthogonal vectors pointing uniformly randomly in \mathbb{R}^n , see [57], and we make sure to generate both slow (eigenvalues close to 100) and fast (eigenvalues close to 1) directions.

Having generated a random covariance matrix C for dimensions $n \in \{2, 4, 8, 16, 32, 64, 128\}$ and having created the resulting dataset as its rank-1 factors, we sample the mean squared loss manifold of the single-layer perceptron using the BAOAB sampler. We use 50,000 steps with a time step size $\varepsilon = 0.125$, inverse temperature $\beta = 1$, friction constant $\gamma = 1$, and covariance blending factor of $\eta = 10$.

We measure the exploration speed in the Gaussian model by looking at the IAT τ per random direction, that we know from the random matrix' eigendecomposition, by projecting it onto each eigenvector and measure the IAT using the package *acor* [24].

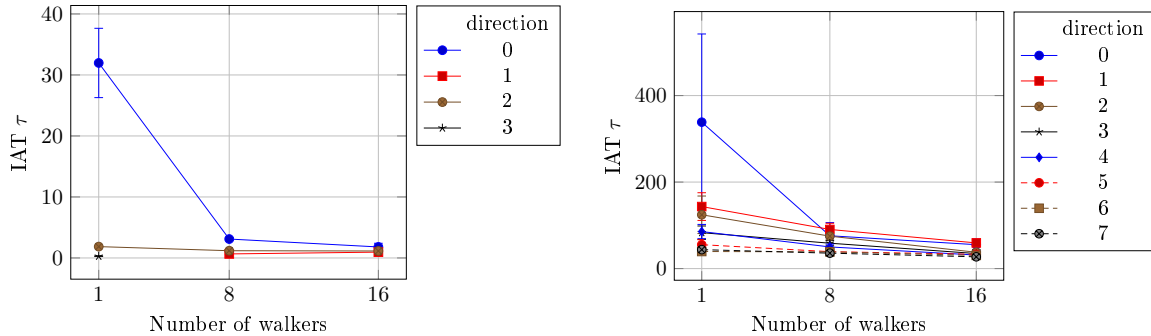


Figure 13: Integrated Autocorrelation Time (IAT) ε over the number of walkers for Gaussian models of dimensions $n \in \{4, 64\}$ where only up to the first 8 directions are shown. Five Sampling runs have been completed for each random covariance matrix and average IAT and standard deviation is shown. With a single walker standard BAOAB sampling is employed, with multiple walkers the EQN method is used.

In Figure 13 we see that using the EQN scheme with 8 or 16 walkers significantly improves the Integrated Autocorrelation Time ε for the slow directions. We note that the fast directions are unaffected. We remind the reader that each walker samples its own trajectory. Hence, we sample up to 16 trajectories in parallel and do so ten times more efficiently because of the reduction in the IATs.

5.3.3 MNIST

We now turn to the MNIST dataset again for a real-world application of the EQN method. We constrain the training dataset to two classes, namely the digits 7 and 9. This results in 11,169 training dataset items for this two-class problem. Again, we employ the same single-layer perceptron as before.

For the IAT computation we have extracted distinct covariance matrices $C_i = \text{cov}(\theta_i^{(n)}, \theta_i^{(n)})$ per walker, obtained the eigendecomposition $C = V\Lambda V^T$, extracted the eigenvectors V_j of the 20 dominant eigenvalues, and projected the walker's trajectory onto these, $\pi_{i,j}(n) = \Theta_i^{(n)} \cdot V_j$. Finally, we calculated the IAT of each $\pi_{i,j}(n)$ using the *acor* package and averaged over all walkers i .

Using walker-individual covariance matrices does not generally change results compared to a single covariance matrix obtained from averaging the trajectory over all walkers. However, it makes them more stable. Because of the high dimensionality of the parameter space $\mathbb{R}^{1,568}$ already small perturbations may cause vectors to become orthogonal⁸. This phenomena is explained by the ‘‘Concentration of Measure’’, see [45]. The eigenvalue spectra themselves are stable for each walker, bounded in deviation by the Bauer-Fike theorem. Note further that the preconditioning matrix $B_i^{(n)}$ is also uniquely defined for each walker.

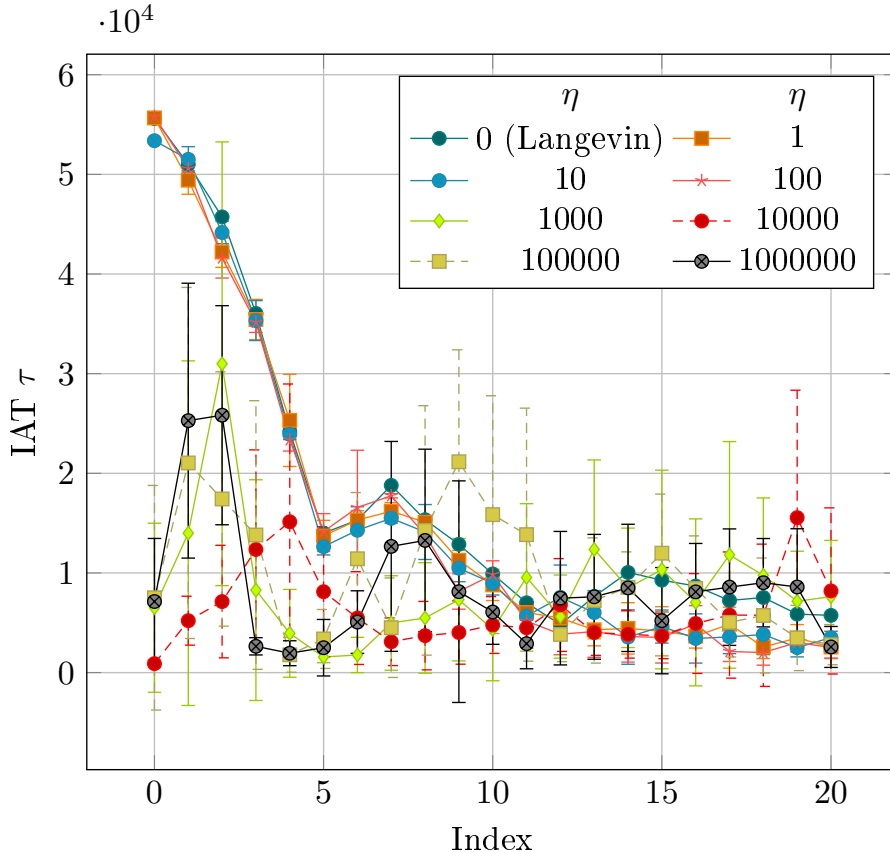


Figure 14: Integrated Autocorrelation Time (IAT) τ for the first 20 covariance eigenvectors over the number of walkers for the MNIST two class problem. We observe a strong improvement of up to a factor of 4 for the slowest Integrated Autocorrelation Time (IAT) which relates to a similar increase in exploration speed, e.g., when using η of 10,000 (EQN) compared to $\eta = 0$ (standard Langevin).

In Figure 14 we then look at the IAT over the first 20 covariance eigenvectors for various values of the covariance blending constant η . We used a fixed number of 8 walkers, a batch size of 550, an inverse temperature constant of $\beta = 10$, the friction constant set to $\gamma = 10$ and a step size $\varepsilon = 0.125$ with the BAOAB sampler. All runs are started from an equilibrated position using SGD with batch size of 550 and a learning rate of 0.1 for 5,000 steps. Note that we recompute the covariance matrix after 10,000 steps. Note that the trajectories were stored with only every 100th sampling step. Hence, the ε values in the Figure have been re-scaled appropriately.

As there is a scaling invariance with respect to the biases of the output layer due to the `argmax` function, we have fixed the biases for the sampling to the values obtained from a prior optimization. At the moment, the EQN implementation cannot deal with such invariances. They represent ‘‘flat valleys’’ in the loss landscape and the walkers will be pushed by the preconditioning along the valley in vain search for its bounds. Such a valley can be hypothesized from the spectrum of the covariance matrix, see Figure 10(b), where the first eigenvalue with $2.1 \cdot 10^6$ is unusually high, and when the EQN does not effectively reduce the IATs although the eigenvalue spectrum indicates it, c.f. [56, p. 281].

We generally observe that especially the first five IAT values are dramatically reduced and see an improvement of up to a factor of 4. The covariance blending can be chosen robustly, up to very high values. This indicates that the covariance matrix itself, despite $L < N$, is already positive definite.

⁸The other way round this becomes: the more dimensions a space has, the more likely it becomes for two random vectors to be orthogonal to each other, see also [52, sect. 7.1].

6 Conclusion

In this article we have presented Thermodynamic Analytics ToolKit (TATi), a thermodynamic sampling and analysis toolkit in *Python* based on *TensorFlow*.

We have implemented several state-of-the-art samplers, based on Brownian, Hamiltonian, and Langevin dynamics, whose software performance and sampling accuracies have been investigated and found to match theoretical expectations. Relying on *TensorFlow*, the implementation efficiently runs in parallel and also on GPU-assisted hardware.

We have looked in our evaluation at the MNIST loss manifold for a single-layer perceptron using softmax cross-entropy. We find that it resembles an anisotropic funnel on the large scale combined with many local minima at its bottom matching well the band of minima bounded from below and exponentially decaying in density with higher loss values predicted in [12]. This motivated an ensemble method employing a number of so-called walkers to obtain a local approximation of the covariance that, when turned into a preconditioner, results in a significant improvement of the sampling speed.

Last but not least, we would like to emphasize that TATi has been developed with extensibility in mind. It contains a framework for rapid prototyping new sampling methods of which we presented a few showcases. We vividly hope for the community to pick up and build upon this software. Future directions in our group consist of Infinite Switch Simulated Tempering (ISST) schemes that would provide an acceleration of the exploration on the small scale as does ensemble quasi-Newton (EQN) on the large scale. Moreover, diffusion maps [13, 11] may be effectively employed in place of (local) covariance to obtain non-linear approximations of the local manifold structure. This may be used for effective exploration where there are many minima separated by potential barriers.

Addendum

A Virial Theorem

The virial is defined as $G = \sum_i^N \theta_i p_i$ with positions θ and momenta p . The virial theorem states that $\frac{dG}{dt} = 0$ which would imply through

$$\frac{dG}{dt} = \sum_i^N p_i \dot{p}_i + \sum_i^N \theta_i \frac{\partial L(\theta)}{\partial \theta_i} \quad (22)$$

that the first term, twice the kinetic energy, equals the negative of the second.

Let us inspect the second term and look at its average over the whole domain using the Gibbs measure with a single degree of freedom ($N = 1$),

$$\frac{\int_{\mathbb{R}} \theta \cdot \nabla L(\theta) \exp(-\beta L(\theta)) d\theta}{\int \exp(-\beta L(\theta)) d\theta},$$

where β is the inverse temperature.

Let us ignore the denominator for the moment and integrate the nominator by parts. We obtain with the derivative $\frac{\partial}{\partial \theta} \exp(-\beta L(\theta)) = -\beta \exp(-\beta L(\theta)) \frac{\partial L(\theta)}{\partial \theta}$,

$$\int_{\mathbb{R}} \theta \cdot \nabla L(\theta) \exp(-\beta L(\theta)) d\theta = \left[\theta \cdot \frac{-1}{\beta} \exp(-\beta L(\theta)) \right] - \int_{\mathbb{R}} 1 \cdot \frac{-1}{\beta} \exp(-\beta L(\theta)) d\theta.$$

If the boundary term vanishes, we obtain

$$\frac{\int_{\mathbb{R}} \frac{1}{\beta} \exp(-\beta L(\theta)) d\theta}{\int_{\mathbb{R}} \exp(-\beta L(\theta)) d\theta} = \frac{1}{\beta}.$$

In other words, the average virial, the second term, would be identical to two times the average kinetic energy $\frac{1}{\beta}$, the first term in (22).

Hence, all that remains is to show that $\left[\theta \cdot \exp(-\beta L(\theta)) \right]_{-\infty}^{\infty} = 0$. Naturally, this holds if $\lim_{|\theta| \rightarrow \infty} L(\theta) \rightarrow \infty$ to the effect that $\exp(-\beta L(\theta)) \rightarrow 0$ faster than $|\theta| \rightarrow \infty$, noting that the exponential increases faster than any polynomial.

In other words, the potential $L(\theta)$ needs to be unbounded and to increase faster than $|\theta|$ for the virial theorem to hold.

A.1 Virial and MNIST

If for the MNIST dataset, a single-layer perceptron with a softmax cross-entropy function is employed, then the virial theorem does not hold.

The output of the single-layer perceptron is $f_i(\theta) = \sum_j W_{i,j}x_j + b_i$ with weight matrix θ and bias vector b , i. e. $\theta = (W, b)$.

As the cross entropy is $-\sum_i y_i \log p_i(f(\theta))$ and the softmax function is $p_i(f(\theta)) = \frac{\exp f_i(\theta)}{\sum_i \exp f_i(\theta)}$, we have $\exp(\beta \sum_i y_i \log p_i(f(\theta))) = \prod_i p_i(f(\theta))^{\beta y_i}$.

Let us set all parameters components to zero except for a single weight component $W_{i,j}$ where at least for one item in the dataset we have $x_j \neq 0$. Then we obtain $W_{i,j}(W_{i,j}x_j)^{\beta y_i}$ as the integrand for this data item (x_i, y_i) and the boundary integral will not converge (to zero) in this case.

Note that this issue could be addressed by the addition of an L_2 regularization strategy.

Acknowledgements

The authors acknowledge funding through a Rutherford fellowship from the Alan Turing Institute in London (R-SIS-003, R-RUT-001) and EPSRC grant no. EP/P006175/1 (Data Driven Coarse Graining using Space-Time Diffusion Maps, B. Leimkuhler PI). The computing resources were provided by a Microsoft Azure Sponsorship award (MS-AZR-0143P).

The authors would also like to express their gratitude to the Research Software Engineering Team of the Alan Turing Institute led by James Hetherington and especially to Martin O'Reilly for support in using the Azure platform. Charles Matthews provided valuable comments on a preliminary draft of the article, leading to a much improved exposition.

References

- [1] A.J. Ballard, R. Das, S. Martiniani, D. Mehta, L. Sagun, J.D. Stevenson, and D.J. Wales. Energy landscapes for machine learning. *Phys. Chem. Chem. Phys.*, 19:12585–12603, 2017. doi: 10.1039/C7CP01108C. URL <http://dx.doi.org/10.1039/C7CP01108C>.
- [2] D. Barber and C. M. Bishop. Ensemble learning in bayesian neural networks. *Neural Networks and Machine Learning*, 168:215?238, 1998.
- [3] R. Bernardi, M. Melo, and K. Schulten. Enhanced sampling techniques in molecular dynamics simulations of biological systems. *Biochimica et Biophysica Acta (BBA) - General Subjects*, 1850(5): 872 – 877, 2015. ISSN 0304-4165. doi: <https://doi.org/10.1016/j.bbagen.2014.10.019>. URL <http://www.sciencedirect.com/science/article/pii/S0304416514003559>. Recent developments of molecular dynamics.
- [4] A. Beskos and A. Stuart. Computational complexity of metropolis-hastings methods in high dimensions. In Pierre L'Ecuyer and Art B. Owen, editors, *Monte Carlo and Quasi-Monte Carlo Methods 2008*, pages 61–71, Berlin, Heidelberg, 2009. Springer Berlin Heidelberg. ISBN 978-3-642-04107-5.
- [5] P.G. Bolhuis, D. Chandler, C. Dellago, and P.L. Geissler. Transition path sampling: Throwing ropes over rough mountain passes, in the dark. *Annual Review of Physical Chemistry*, 53(1):291–318, 2002. doi: 10.1146/annurev.physchem.53.082301.113146. URL <https://doi.org/10.1146/annurev.physchem.53.082301.113146>. PMID: 11972010.
- [6] D. Bone, M. Goodwin, M. Black, C.-C. Lee, K. Audhkhasi, and S. Narayanan. Applying machine learning to facilitate autism diagnostics: pitfalls and promises. *J. Autism Dev. Disord.*, 45:1121–1136, 2015. URL <https://doi.org/10.1007/s10803-014-2268-6>.
- [7] L. Bottou, F. Curtis, and J. Nocedal. Optimization methods for large-scale machine learning. *SIAM Review*, 60(2):223–311, 2018. doi: 10.1137/16M1080173. URL <https://doi.org/10.1137/16M1080173>.
- [8] N. Bou-Rabee and H. Owhadi. Long-run accuracy of variational integrators in the stochastic context. *SIAM J. Num. Anal.*, 48(1):278–297, 2010.
- [9] P. Chaudhari, A. Choromanska, S. Soatto, Y. LeCun, C. Baldassi, C. Borgs, J. Chayes, L. Sagun, and R. Zecchina. Entropy-sgd: Biasing gradient descent into wide valleys. *arXiv Prepr. arXiv1611.01838*, 2016.

- [10] T. Chen, E. Fox, and C. Guestrin. Stochastic gradient hamiltonian monte carlo. In *Int. Conf. Mach. Learn.*, pages 1683–1691, 2014.
- [11] E. Chiavazzo, R.R. Coifman, R.a Covino, C.W. Gear, A.S. Georgiou, G. Hummer, and I.G. Kevrekidis. iMapD: intrinsic Map Dynamics exploration for uncharted effective free energy landscapes. *PNAS*, 2017.
- [12] A. Choromanska, M. Henaff, M. Mathieu, G. Ben Arous, and Y. LeCun. The Loss Surfaces of Multilayer Networks. In *Proc. Mach. Learn. Res.*, pages 92–204, 2015. ISBN 1412.0233. URL <http://proceedings.mlr.press/v38/choromanska15.html>.
- [13] R. Coifman and S. Lafon. Diffusion maps. *Appl. Comput. Harmon. Anal.*, 21(1):5–30, 2006. ISSN 10635203. doi: 10.1016/j.acha.2006.04.006.
- [14] T.H. Cormen, C.E. Leiserson, R.L. Rivest, and C. Stein. *Introduction to Algorithms*. MIT Press, 2. edition, 2001. ISBN 0-262-03293-7.
- [15] J.V. Dillon, I. Langmore, D. Tran, E. Brevdo, S. Vasudevan, D. Moore, B. Patton, A. Alemi, M. Hoffman, and R.A. Saurous. TensorFlow Distributions. 2017.
- [16] Laurent Dinh, Razvan Pascanu, Samy Bengio, and Yoshua Bengio. Sharp minima can generalize for deep nets. In Doina Precup and Yee Whye Teh, editors, *Proceedings of the 34th International Conference on Machine Learning*, volume 70 of *Proceedings of Machine Learning Research*, pages 1019–1028, International Convention Centre, Sydney, Australia, 06–11 Aug 2017. PMLR. URL <http://proceedings.mlr.press/v70/dinh17b.html>.
- [17] Felix Draxler, Kambis Veschgini, Manfred Salmhofer, and Fred Hamprecht. Essentially no barriers in neural network energy landscape. In Jennifer Dy and Andreas Krause, editors, *Proceedings of the 35th International Conference on Machine Learning*, volume 80 of *Proceedings of Machine Learning Research*, pages 1309–1318. PMLR, 10–15 Jul 2018. URL <http://proceedings.mlr.press/v80/draxler18a.html>.
- [18] J. Duchi, E. Hazan, and Y. Singer. Adaptive subgradient methods for online learning and stochastic optimization. *The Journal of Machine Learning Research*, 12:2121–2159, 2011. ISSN 15324435. doi: 10.1109/CDC.2012.6426698. URL http://portal.acm.org/ft_gateway.cfm?id=2021068&ftid=1013134&coll=DL&d1=GUIDE&CFID=346380592&CFTOKEN=89823863&0Ahttp://portal.acm.org/citation.cfm?id=1953048.2021068&coll=DL&d1=GUIDE&CFID=346380592&CFTOKEN=89823863&0Ahttp://dl.acm.org/citation.cfm?id=2021068&0Ahttp://dl.acm.org/citation.cfm?id=2021068.
- [19] D.B. Dunson. Statistics in the big data era: Failures of the machine. *Stat. Probab. Lett.*, 136:4–9, 2018.
- [20] A. Durmus and E. Moulines. High-dimensional bayesian inference via the unadjusted langevin algorithm. 2018. URL <https://arxiv.org/pdf/1805.01648v3.pdf>.
- [21] R. Elber. Perspective: Computer simulations of long time dynamics. *J. Chem. Phys.*, 144:060901, 2016.
- [22] Y. Gal. *Uncertainty in Deep Learning*. PhD thesis, Cambridge University, 2016.
- [23] I.J. Goodfellow, O. Vinyals, and A.M. Saxe. Qualitatively characterizing neural network optimization problems. In *Int. Conf. Learn. Represent.*, 2014. URL <http://arxiv.org/abs/1412.6544>.
- [24] J. Goodman. *ACOR package*, 2009. URL <http://www.math.nyu.edu/faculty/goodman/software/>.
- [25] J. Goodman and J. Weare. Ensemble samplers with affine invariance. *Commun. Appl. Math. Comput. Sci.*, 5(1):65–80, jan 2010. ISSN 2157-5452. doi: 10.2140/camcos.2010.5.65. URL <http://msp.org/camcos/2010/5-1/p04.xhtml>.
- [26] C.L. Gomez, I. Santos, J.G. de la Puerta, P.G. Bringas, and P. Galan-Garcia. Supervised machine learning for the detection of troll profiles in twitter social network: application to a real case of cyberbullying. *Logic Journal of the IGPL*, 24(1):42–53, 10 2015. ISSN 1367-0751. doi: 10.1093/jigpal/jzv048. URL <https://dx.doi.org/10.1093/jigpal/jzv048>.

- [27] B.D. Haeffele and R. Vidal. Global optimality in neural network training. *Proc. - 30th IEEE Conf. Comput. Vis. Pattern Recognition, CVPR 2017*, 2017-Janua(3):4390–4398, 2017. doi: 10.1109/CVPR.2017.467.
- [28] M. Hardt, B. Recht, and Y. Singer. Train faster, generalize better: Stability of stochastic gradient descent. *arXiv Prepr. arXiv1509.01240*, 2015.
- [29] K. He, X. Zhang, S. Ren, and J. Sun. Deep residual learning for image recognition. In *Proc. IEEE Conf. Comput. Vis. pattern Recognit.*, pages 770–778, 2016.
- [30] G. Hinton, N. Srivastava, K. Swersky, and T. Tieleman. rmsprop: Divide the gradient by a running average of its recent magnitude, 2014.
- [31] G.E. Hinton and D. Van Camp. Keeping the neural networks simple by minimizing the description length of the weights. In *Proceedings of the sixth annual conference on Computational learning theory*, page 5?13. ACM, 1993.
- [32] S. Hochreiter and J. Schmidhuber. Flat Minima. *Neural Comput.*, 9(1):1–42, jan 1997. ISSN 0899-7667. doi: 10.1162/neco.1997.9.1.1. URL <http://www.mitpressjournals.org/doi/10.1162/neco.1997.9.1.1>.
- [33] E. Hoffer, I. Hubara, and D. Soudry. Train longer, generalize better: closing the generalization gap in large batch training of neural networks. In *Neur. Inf. Proc. Sys.*, 2017.
- [34] D.J. Im, M. Tao, and K. Branson. An empirical analysis of the optimization of deep network loss surfaces. pages 1–21, dec 2016. URL <http://arxiv.org/abs/1612.04010>.
- [35] K. Johnson, J. Torres Soto, B. Glicksberg, K. Shameer, R. Miotto, M. Ali, E. Ashley, and J. Dudley. Artificial intelligence in cardiology. *Journal of the American College of Cardiology*, 71:2668–2679, 2018. ISSN 0735-1097. URL <https://doi.org/10.1016/j.jacc.2018.03.521>.
- [36] K. Kadau, T.C. Germann, and P.S. Lomdahl. Large-scale molecular-dynamics simulation of 19 billion particles. *International Journal of Modern Physics C*, 15(01):193–201, 2004. doi: 10.1142/S0129183104005590. URL <https://doi.org/10.1142/S0129183104005590>.
- [37] K. Kawaguchi, L. Kaelbling, and Y. Bengio. Generalization in Deep Learning. 2017. ISSN 10495258. URL <http://arxiv.org/abs/1710.05468>.
- [38] D.P. Kingma and J. Ba. Adam: A method for stochastic optimization. *arXiv Prepr. arXiv1412.6980*, 2014.
- [39] M.L. Klein and W. Shinoda. Large-scale molecular dynamics simulations of self-assembling systems. *Science*, 321(5890):798–800, 2008. ISSN 0036-8075. doi: 10.1126/science.1157834. URL <http://science.sciencemag.org/content/321/5890/798>.
- [40] A. Krizhevsky, I. Sutskever, and G.E. Hinton. Imagenet classification with deep convolutional neural networks. In *Adv. Neural Inf. Process. Syst.*, pages 1097–1105, 2012.
- [41] Y. LeCun. MNIST dataset. URL <http://yann.lecun.com/exdb/mnist/>.
- [42] Y. LeCun, I. Kanter, and S.A. Solla. Eigenvalues of covariance matrices: Application to neural-network learning. *Phys. Rev. Lett.*, 66(18):2396–2399, 1991. ISSN 00319007. doi: 10.1103/PhysRevLett.66.2396.
- [43] Y. LeCun, L. Bottou, Y. Bengio, and P. Haffner. Gradient-based learning applied to document recognition. *Proc. IEEE*, 86(11):2278–2324, 1998. ISSN 00189219. doi: 10.1109/5.726791. URL <http://ieeexplore.ieee.org/document/726791/>.
- [44] Y. LeCun, Y. Bengio, and G. Hinton. Deep learning. *Nature*, 521(7553):436, 2015.
- [45] M. Ledoux. *The concentration of measure phenomenon*. Mathematical surveys and monographs ; no. 89. American Mathematical Society, Providence, R.I., 2001. ISBN 0821828649.
- [46] B. Leimkuhler and C. Matthews. Rational Construction of Stochastic Numerical Methods for Molecular Sampling. *Appl. Math. Res. eXpress*, 2013(1):34–56, 2012. doi: 10.1093/amrx/abs010.

- [47] B. Leimkuhler and C. Matthews. *Molecular Dynamics With Deterministic and Stochastic Numerical Methods*. Springer International Publishing, Heidelberg, 1st edition, 2015.
- [48] B. Leimkuhler and X. Shang. Adaptive Thermostats for Noisy Gradient Systems. *SIAM Journal on Scientific Computing*, 38(2):A712–A736, jan 2016. ISSN 1064-8275. doi: 10.1137/15M102318X. URL <https://epubs-siam-org.ezproxy.is.ed.ac.uk/doi/abs/10.1137/15M102318X><http://epubs.siam.org/doi/10.1137/15M102318X>.
- [49] B. Leimkuhler, C. Matthews, and G. Stoltz. The computation of averages from equilibrium and nonequilibrium Langevin molecular dynamics. *IMA J. Numer. Anal.*, 36(1):13–79, 2015.
- [50] T. Lelièvre, M. Rousset, and G. Stoltz. *Free Energy Computations*. IMPERIAL COLLEGE PRESS, 2010. doi: 10.1142/p579. URL <https://www.worldscientific.com/doi/abs/10.1142/p579>.
- [51] C. Li, C. Chen, D. Carlson, and L. Carin. Preconditioned Stochastic Gradient Langevin Dynamics for Deep Neural Networks. In *Proceedings of the 30th Conference on Artificial Intelligence (AAAI 2016)*, pages 1788–1794, 2015. ISBN 9781577357605. URL <http://arxiv.org/abs/1512.07666>.
- [52] H. Li, Z. Xu, G. Taylor, C. Studer, and T. Goldstein. Visualizing the Loss Landscape of Neural Nets. 2018. URL <http://arxiv.org/abs/1712.09913>.
- [53] R. Livni, S. Shalev-Shwartz, and O. Shamir. On the Computational Efficiency of Training Neural Networks. In *Adv. Neural Inf. Process. Syst. 27*, pages 855–863, 2014.
- [54] D.J. MacKay. A practical bayesian framework for backpropagation networks. *Neural Computation*, 4:448?472, 1992.
- [55] C. Matthews and J. Weare. Langevin Markov Chain Monte Carlo with stochastic gradients. *arXiv Prepr. arXiv1805.08863*, 2018.
- [56] C. Matthews, J. Weare, and B. Leimkuhler. Ensemble preconditioning for Markov chain Monte Carlo simulation. *Stat. Comput.*, 28(2):277–290, 2018. ISSN 0960-3174. doi: 10.1007/s11222-017-9730-1. URL <http://arxiv.org/abs/1607.03954>.
- [57] F. Mezzadri. How to generate random matrices from the classical compact groups. *Not. AMS*, 54: 592–604, 2007.
- [58] Radford M Neal. MCMC Using Hamiltonian Dynamics. In *Handb. Markov Chain Monte Carlo*, chapter 5, pages 113–162. Chapman and Hall, 2011.
- [59] R.M. Neal. Bayesian training of backpropagation networks by the hybrid monte carlo method. Technical Report CRG-TR-92-1, Dept. of Computer Science, University of Toronto, 1992.
- [60] J. Nocedal and S.J. Wright. *Numerical Optimization*. Springer-Verlag, New York, 1. edition, 1999. ISBN 0-387-98793-2.
- [61] A. Paszke, S. Gross, S. Chintala, G. Chanan, E. Yang, Z. DeVito, Z. Lin, A. Desmaison, L. Antiga, and A. Lerer. Automatic differentiation in pytorch. *NIPS 2017 Autodiff Workshop*, 2017.
- [62] S. Patterson and Y.-W. Teh. Stochastic gradient Riemannian Langevin dynamics on the probability simplex. In *Adv. Neural Inf. Process. Syst.*, pages 3102–3110, 2013.
- [63] C.P. Robert. *The Metropolis-Hastings Algorithm*, pages 1–15. American Cancer Society, 2015. ISBN 9781118445112. doi: 10.1002/9781118445112.stat07834. URL <https://onlinelibrary.wiley.com/doi/abs/10.1002/9781118445112.stat07834>.
- [64] Lorenzo Rosasco, Ernesto De Vito, Andrea Caponnetto, Michele Piana, and Alessandro Verri. Are loss functions all the same? *Neural Computation*, 16(5):1063–1076, 2004. doi: 10.1162/089976604773135104. URL <https://doi.org/10.1162/089976604773135104>.
- [65] Itay Safran and Ohad Shamir. On the quality of the initial basin in overspecified neural networks. In *Proceedings of the 33rd International Conference on International Conference on Machine Learning - Volume 48, ICML’16*, pages 774–782. JMLR.org, 2016. URL <http://dl.acm.org/citation.cfm?id=3045390.3045473>.

- [66] N. Sebe, I. Cohen, A. Garg, and T.S. Huang. Machine learning in computer vision. In *Computational Imaging and Vision*, 2005.
- [67] X. Shang, Z. Zhu, B. Leimkuhler, and A. Storkey. Covariance-controlled adaptive Langevin thermostat for large-scale Bayesian sampling. In *Adv. Neural Inf. Process. Syst.*, pages 37–45, 2015.
- [68] R. Smith. *Uncertainty Quantification: Theory, Implementation, and Applications*. SIAM, 2013.
- [69] M. Soltanolkotabi, A. Javanmard, and J.D. Lee. Theoretical insights into the optimization landscape of over-parameterized shallow neural networks. *IEEE Transactions on Information Theory*, 65(2):742–769, Feb 2019. ISSN 0018-9448. doi: 10.1109/TIT.2018.2854560.
- [70] S.J. Vollmer, K.C. Zygalakis, and Y.-W. Teh. Exploration of the (non-) asymptotic bias and variance of stochastic gradient langevin dynamics. *J. Mach. Learn. Res.*, 17(1):5504–5548, 2016.
- [71] M. Welling and Y.-W. Teh. Bayesian Learning via Stochastic Gradient Langevin Dynamics. *Proc. 28th Int. Conf. Mach. Learn.*, pages 681–688, 2011. doi: 10.1515/jip-2012-0071.
- [72] T. Young, D. Hazarika, S. Poria, and E. Cambria. Recent trends in deep learning based natural language processing. *CoRR*, abs/1708.02709, 2017. URL <http://arxiv.org/abs/1708.02709>.
- [73] C. Zhang and Y. Ma. *Ensemble Machine Learning*. Springer US, Boston, MA, 2012. ISBN 978-1-4419-9325-0. doi: 10.1007/978-1-4419-9326-7. URL <http://link.springer.com/10.1007/978-1-4419-9326-7>.
- [74] G. Zhao, J.R. Perilla, E.L. Yufenyuy, X. Meng, B. Chen, J. Ning, J. Ahn, A.M. Greenborn, K. Schulten, C. Aiken, and P. Zhang. Mature hiv-1 capsid structure by cryo-electron microscopy and all-atom molecular dynamics. *Nature*, 497:643?646, 2013.